INVESTIGATION OF THE CORROSION PROPAGATION CHARACTERISTICS OF NEW METALLIC REINFORCING BARS

JOHN R. SCULLY, Ph.D.
Professor
Department of Materials Science and Engineering
University of Virginia

MICHAEL F. HURLEY
Graduate Research Assistant
Department of Materials Science and Engineering
University of Virginia

VTRC
Virginia Transportation
Research Council

Standard Title Page - Report on State Project

Report No.	Report Date	No. Pages	Type Report: Final Contract	Project No. 73184
VTRC 07-CR9	February 2007	61	Period Covered:	Contract No.

Title: Investigation of the Corrosion Propagation Characteristics of New Metallic Reinforcing Bars	Key Words: Corrosion, reinforcement, concrete, steel, bridge
Authors: John R. Scully, Ph.D. and Michael F. Hurley, Ph.D.	
Performing Organization Name and Address: Virginia Transportation Research Council 530 Edgemont Road Charlottesville, VA 22903	
Sponsoring Agencies' Name and Address: Virginia Department of Transportation 1401 E. Broad Street Richmond, VA 23219	
Supplementary Notes	

Abstract

The threshold chloride concentrations for solid 316LN stainless steel, 316L stainless steel clad, 2101 LDX duplex stainless steel, MMFX-2 (Fe-9%Cr), and carbon steel (ASTM A615) rebars were investigated through laboratory tests in saturated $Ca(OH)_2$ + NaCl solutions.

- The chloride threshold for carbon steel was found to be less than a Cl^-/OH^- molar ratio of 1, which was consistent with the literature. Solid 316LN stainless steel rebar in a pickled condition was found to have a much higher chloride threshold (i.e., threshold Cl^-/OH^- ratio > 20) than carbon steel ($0.25 < Cl^-/OH^- < 0.34$). Pickled 2101 LDX (UNS S32101) had a chloride threshold Cl^-/OH^- ratio of 9.7 and un-aged pickled MMFX-2 (Fe-9.3% Cr) had a chloride threshold Cl^-/OH^- ratio of 4.9. 316L stainless steel clad rebar possessed a chloride threshold Cl^-/OH^- ratio of 4.9 with intact cladding.

- Surface preparation, duration of period exposed to a passivating condition in $Ca(OH)_2$ solution prior to introduction of chloride, and presence of cladding defects all affected the threshold chloride concentration obtained. For instance, the presence of mill scale on any of the corrosion-resistant materials reduced the chloride threshold to approximately that of carbon steel. Therefore, pickling is highly recommended in any reinforcement substitute. The chloride threshold for 316L clad rebar was also highly dependent on any defects that exposed the carbon steel core. It was similar to solid stainless steel when intact and when defective, it was similar to that of carbon steel rebar.

- The model-predicted extension of time until corrosion initiation in concrete could extend to 100 years or more in a pickled condition by using rebar materials such as 316L or 316LN stainless steel with a higher corrosion resistance.

- Corrosion propagation studies indicated that while radial propagation might be similar on all materials once local corrosion was initiated, lateral spread of corrosion would be limited on clad and solid stainless steels. This finding has significant engineering ramifications as the depth of penetration of corrosion of stainless steel reinforcement would in this case have to be far more extensive in order to damage overlying concrete by oxide wedging.

- Lastly, corrosion products were found to be either similar on all materials or, if different, to possess similar molar volumes alleviating concerns that oxide wedging could be worse on new candidate rebar materials.

These findings indicate the total corrosion lifetime, given by the time until initiation and the time of propagation until concrete damage, can be improved to well over 100 years by using pickled stainless steel. The VTRC should investigate use of highly alloyed stainless steel in metropolitan applications where access for repair and maintenance is limited.

FINAL CONTRACT REPORT

**INVESTIGATION OF THE CORROSION PROPAGATION CHARACTERISTICS
OF NEW METALLIC REINFORCING BARS**

John R. Scully, Ph.D.
Professor
Department of Materials Science and Engineering
University of Virginia

Michael F. Hurley, Ph.D.
Graduate Research Assistant
Department of Materials Science and Engineering
University of Virginia

ABSTRACT

The threshold chloride concentrations for solid 316LN stainless steel, 316L stainless steel clad, 2101 LDX duplex stainless steel, MMFX-2 (Fe-9%Cr), and carbon steel (ASTM A615) rebars were investigated through laboratory tests in saturated $Ca(OH)_2$ + NaCl solutions.

- The chloride threshold for carbon steel was found to be less than a Cl^-/OH^- molar ratio of 1, which was consistent with the literature. Solid 316LN stainless steel rebar in a pickled condition was found to have a much higher chloride threshold (i.e., threshold Cl^-/OH^- ratio > 20) than carbon steel ($0.25 < Cl^-/OH^- < 0.34$). Pickled 2101 LDX (UNS S32101) had a chloride threshold Cl^-/OH^- ratio of 9.7 and un-aged pickled MMFX-2 (Fe-9.3% Cr) had a chloride threshold Cl^-/OH^- ratio of 4.9. 316L stainless steel clad rebar possessed a chloride threshold Cl^-/OH^- ratio of 4.9 with intact cladding.

- Surface preparation, duration of period exposed to a passivating condition in $Ca(OH)_2$ solution prior to introduction of chloride, and presence of cladding defects all affected the threshold chloride concentration obtained. For instance, the presence of mill scale on any of the corrosion-resistant materials reduced the chloride threshold to approximately that of carbon steel. Therefore, pickling is highly recommended in any reinforcement substitute. The chloride threshold for 316L clad rebar was also highly dependent on any defects that exposed the carbon steel core. It was similar to solid stainless steel when intact and when defective, it was similar to that of carbon steel rebar.

- The model-predicted extension of time until corrosion initiation in concrete could extend to 100 years or more in a pickled condition by using rebar materials such as 316L or 316LN stainless steel with a higher corrosion resistance.

- Corrosion propagation studies indicated that while radial propagation might be similar on all materials once local corrosion was initiated, lateral spread of corrosion would be limited on clad and solid stainless steels. This finding has significant engineering ramifications as the depth of penetration of corrosion of stainless steel reinforcement would in this case have to be far more extensive in order to damage overlying concrete by oxide wedging.

- Lastly, corrosion products were found to be either similar on all materials or, if different, to possess similar molar volumes alleviating concerns that oxide wedging could be worse on new candidate rebar materials.

These findings indicate the total corrosion lifetime, given by the time until initiation and the time of propagation until concrete damage, can be improved to well over 100 years by using pickled stainless steel. The VTRC should investigate use of highly alloyed stainless steel in metropolitan applications where access for repair and maintenance is limited.

FINAL CONTRACT REPORT

INVESTIGATION OF THE CORROSION PROPAGATION CHARACTERISTICS
OF NEW METALLIC REINFORCING BARS

John R. Scully, Ph.D.
Professor
Department of Materials Science and Engineering
University of Virginia

Michael F. Hurley, Ph.D.
Graduate Research Assistant
Department of Materials Science and Engineering
University of Virginia

INTRODUCTION

Corrosion of Rebar in Concrete

Overview

In many parts of the U.S., where de-icing salts are used in the winters, corrosion of reinforcing steel bars is the prevalent cause of the deterioration − often prematurely − of concrete bridges. Prompted by rapidly rising highway construction costs, bridge designers have raised their design goal for new concrete bridges from 50-years to at least 75-years service life for regular bridges and 100-years service life for major bridges (McDonald et al., 1998).

Corrosion of conventional carbon steel rebar in reinforced concrete has become a major concern for the Department of Transportation due to the resulting decrease in lifetime of concrete structures and cost associated with repair (Koch et al., 2001). Repair costs associated with the corrosion of reinforcing steel are estimated at over $8 billion (Koch et al., 2001). Theoretically, carbon steel rebar is immune to corrosion when embedded in concrete due the high alkalinity created by the concrete environment. Unfortunately, this is not always the case due to surrounding environmental conditions. Typically, passivity of the embedded rebar is lost due to sufficient accumulation of chloride ions and dissolved oxygen introduced from the surrounding environment. These conditions are encountered in tropical environments due to exposure to seawater and areas where deicing salts are used heavily to prevent adverse driving conditions in the winter. The critical chloride concentration that enables corrosion initiation is known as the chloride threshold and is typically expressed as weight per volume of concrete (kg/m^3) or chloride to hydroxide ion ratio (Cl^-/OH^-) in pore solution (Li and Sagüés, 2001).

Once corrosion has initiated at the rebar surface due to chloride ion ingress, corrosion products (that occupy a larger volume than the parent metal) begin to accumulate. Formation of corrosion products at the rebar interface creates tensile stresses in the concrete that eventually lead to cracking of the surrounding concrete. This creates an easier pathway for the introduction

of aggressive species and promotes further rebar corrosion. Continued corrosion propagation of the rebar over time renders the composite structurally deficient, necessitating structure closures and repairs.

The prospect of building new concrete bridges that will last much longer than existing bridges by using the new alloyed reinforcing bars prompted the initiation, in 1999, of investigations at the Virginia Transportation Research Council and the University of Virginia to ascertain the added corrosion protection expected of these new bars (Scully et al., 2003). Although carbon steel reinforcement has performed adequately in non-aggressive environments with proper rebar placement and high quality concrete cover depth, use of carbon steel in aggressive environments does not meet current structure lifetime design goals (McDonald et al., 1998). Moreover, use of epoxy coated rebar often only offers modest extension of life if the epoxy is damaged during installation (Clear, 1996; McDonald et al., 1996). Therefore, the use of solid stainless steel, clad stainless steel and other alloyed steels instead of carbon steel rebars are being considered with the lifetime design goal of 75-100 years.

In addition to the stainless steel clad bar (16% Cr, 10.2% Ni, 2.7% Mo, 1.3% Mn); a carbon steel bar, two solid stainless steels (316LN austenitic, 17.8% Cr, 11.6% Ni, 2.8% Mo, 1.6% Mn and 2101 duplex, 21.2% Cr, 1.6% Ni, 2.7% Mo, 4.8% Mn) and MMFX-2 (9.3% Cr, 0.089% Ni, 0.023% Mo, 0.46% Mn) bars were included in the present study for comparison purposes. However, some observations in the aforementioned investigation have hinted that the different bars may also have different corrosion propagation characteristics due to the variations in alloy microstructure and chemistry, i.e., prevalent rate of corrosion, mode of corrosion (uniform or local) along the bar, etc. Visual observation of chloride threshold samples post-testing revealed that stainless steel bars typically were limited to very localized corrosion attack whereas the carbon steel bars showed evidence of global depassivation. Therefore, both propagation area or morphology and rates of attack may vary depending on bar composition and microstructure. This suggests that a bar that exhibits the best or longest initiation phase may not necessarily exhibit the best behavior during the propagation phase. Further, this would then suggest that the influence of the propagation phase characteristics of each bar should also be taken into consideration in determination of its overall service life. For this purpose, the rate at which and the manner with which corrosion propagates on each of these new bars and the corresponding extent with which the corrosion damages the concrete via corrosion product formation need to be investigated.

Corrosion Initiation, Propagation, and Induced Concrete Spalling

For analysis of the life-cycle cost of any concrete bridge member exposed to chloride intrusion, the service life is considered to be the sum of the corrosion initiation and propagation phases, as illustrated in Figure 1 (Tuutti, 1982). The corrosion initiation phase is the time required from the day the structure is put into service for chloride ions to diffuse from the surface, through pores to the embedded rebar surface, eventually accumulating to a critical concentration sufficient to initiate corrosion on the bars. The transport rate of chloride is concrete material dependent while the chloride threshold is rebar material dependent (Hausmann, 1967). If no cracks are present – especially those that are wider than 0.3 mm (0.01 in.) – the length of the initiation phase is a function of the permeability of the concrete, the concrete cover, the type of cementitious materials used, and the corrosion resistance of the bars (Houston et al.,

1972; Ryell and Richardson, 1972). However, when wide cracks are present in the concrete deck, then corrosion resistance of the bars becomes the only factor that has any practical influence on the corrosion initiation phase. The threshold chloride concentration and the time to corrosion initiation are unknown for alternative rebar materials.
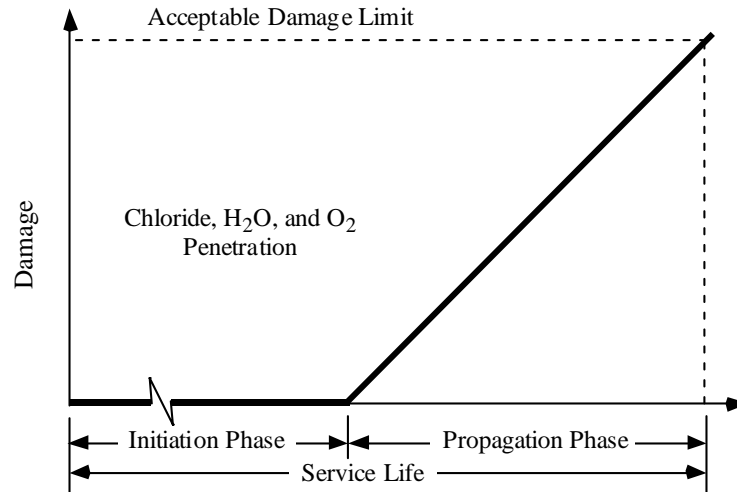
Figure 1. Service life prediction model for reinforced concrete bridges exposed to chloride, after Tuutti (Tuutti, 1982).

The propagation phase is the time required for corrosion on the bars to propagate to the extent at which either the load capacity of the structural elements is inadequate or it is more economical to replace the elements than to keep on repairing the resulting concrete damage, i.e., cracking due to excessive corrosion product formation. The propagation characteristics of new alternative reinforcement materials are also unknown. There are three aspects of the propagation stage of reinforcing bar corrosion that are investigated in this study. The first is the characteristic morphology of corrosion propagation on each of the new bars once its chloride threshold level is exceeded. Propagation morphology defines the area of corrosion propagation or effective length of the region along the bar that actively corrodes compared to the portion that remains passive. It is suspected that, once its chloride threshold is reached and pits are formed, low carbon steel would exhibit rapid global or widespread lateral depassivation. On the other hand, because of their high corrosion resistance in acidified solutions, stainless steels would likely form high-aspect-ratio pits with little risk of global depassivation (Jones, 1996). At issue is whether isolated formation of corrosion products that possess a relatively small footprint could induce spalling of concrete due to corrosion product wedging. Based on its composition, the new 2101 LDX (21.2% Cr, 1.6% Ni, 2.7% Mo, 4.8% Mn) may behave like a stainless steel (Sedriks, 1996); on the other hand, the behavior of new "hybrid" steels such as MMFX–2 (9.3% Cr, 0.089% Ni, 0.023% Mo, 0.46% Mn) is completely unknown.

The second aspect of corrosion propagation behavior that must be characterized is the rate of propagation both parallel to the surface (lateral) and normal to the surface (radial) of the rebar. In one study on carbon steel bars, it was found that the critical depth of attack required to

3

crack concrete, X_{crit}, was a function of the specimen diameter, 2r, and concrete cover thickness, C, as well as the length of anodic region along the axis of the bar, L (Torres-Acosta and Sagüés, 2000). Hence, as the length of anodic region of corrosion propagation, L, increases, X_{crit} decreases. This implies that both the rate of penetration and lateral area of corrosive attack are important factors determining the risk of concrete cracking. Therefore, the corrosion morphology as well as the propagation rate per unit area (both radial and lateral) must be understood for candidate rebar materials. The former factor determines the characteristic time required to reach X_{crit} of each bar, while the later factor influences the former.

The third aspect of corrosion propagation relevant to concrete damage is the formation of corrosion product(s) that occupy a larger molar volume than the molar volume of the parent metal. The accumulation rate of corrosion products, the crystal nano-structure, and atoms per unit volume in such a nanostructure (e.g., molar volume) of the corrosion product compared to the molar volume in the metallic phase together determine the possible extent of concrete damage. The propagation rate determines the metal-to-oxide conversion rate, and the oxide structure identification and density of the corrosion products aid in determination of the propensity to damage and crack concrete. The corrosion product composition, structure and density are unknown for new alloys and must be characterized under conditions relevant to rebar corrosion or dismissed as being substantially similar to the corrosion products formed on carbon steel when corroded in concrete.

Corrosion Resistant Rebar to Improve Concrete Structure Lifetimes

Attributes of Corrosion Resistant Rebar Beneficial for Corrosion in Concrete and Extension of Structure Lifetimes

Cr Alloyed Rebar

Stainless steel is an attractive alternative to carbon steel due to its inherently higher corrosion resistance that eliminates the need for an epoxy coating. The term stainless steel refers to a class of steels with alloying elements added to improve corrosion resistance, mainly having a chromium content greater than 12% (Jones, 1996). A naturally occurring iron-chromium rich oxide layer forms. The uniform corrosion resistance improvements afforded by the chromium addition can be predicted by thermodynamic principles, as illustrated by Pourbaix diagrams (Pourbaix, 1974). The corrosion resistance can be further increased by the introduction of additional alloying elements such as: nickel, molybdenum, titanium, as well as others (Sedriks, 1996). Fe-Cr-Ni alloys extend the thermodynamic region of passivity to lower pH levels than possible in Fe-C-Mn alloys (Sedriks, 1996). Moreover, it is expected from the literature that Fe-Cr-Ni alloys would also possess very high resistances to pit and crevice type corrosion that has been observed on carbon steel under aggregate in concrete (Wilde, 1972; Sedriks, 1996). Stainless steel might be immune from these forms of localized corrosion except at the most severe chloride concentrations in concrete and the most oxidizing conditions (Szklarska-Simialowska, 2005). The degree of immunity is governed by the alloying content. Speculatively, in the event of localized stainless steel rebar corrosion, attack may propagate more quickly due to greater acidification as a result of metal cation hydrolysis but might be limited to a much smaller area than on carbon steel based on pitting behavior or the small crevice formed by aggregate. Localized corrosion might detrimentally impact the mechanical properties of the rebar, but the

effect of voluminous oxide formation on concrete spalling might be minimal because corrosion products would be limited to small areas instead of being distributed more uniformly over the entire surface of the rebar. Thus, if corrosion products possessed the same molar volume, as in the case of carbon steel, L in the Torres-Acosta analysis would be much smaller and X_{crit} would be much larger.

The major drawback regarding employing stainless steel rebar in construction applications is the increased cost over carbon steel. The projected increase in materials cost of stainless steel rebar is approximately 4-8 times greater than carbon steel rebar depending on stainless steel grade (Nurnberger, 1996). However, the projected lifetime costs of using stainless steel are likely lower than carbon steel rebar, due to the extended structure lifetimes without the need for costly repair and rehabilitation projects (McDonald et al., 1998). However, the actual degree of extension of lifetimes must be established and for this can be accomplished, baseline properties must be established.

Stainless Steel Clad Rebar

Austenitic stainless steel cladding over carbon steel is an attractive alternative to solid stainless steel from both a cost and corrosion mitigation standpoint. One would ideally gain the resistance to corrosion of solid stainless steel at a fraction of the cost of solid single-phase stainless steel. Of great interest is the resulting corrosion behavior when a break in the clad layer exists, exposing the carbon steel core, is incurred. This exceptional, but critical case could be realized through either: significant localized corrosion through the clad layer or mechanically induced damage (e.g., construction site handling or unsealed cut ends). The two situations that expose the carbon steel core are fundamentally different. Pitting corrosion creates a localized aggressive environment high in chloride and low in pH due to Cr^{+3} hydrolysis (Jones, 1996). Chromium ions liberated from the parent stainless steel hydrolyze to create local acidification at the corrosion site resulting in rapid galvanic corrosion of exposed carbon steel in an acidified pit type environment. In the case of a mechanical defect, the localized acidified environment is absent, but the possibility still exists for galvanic corrosion under conditions where the chloride content at the interface is above the critical chloride threshold for the underlying carbon steel but below that of stainless steel. Regarding corrosion initiation, the weakest link in the system will determine the chloride threshold.

PURPOSE AND SCOPE

Motivation

There is a significant increase in cost associated with the implementation of a corrosion resistant rebar substitution. In order to justify use of these rebars it is necessary to investigate thoroughly the corrosion characteristics. This project was undertaken to investigate potential benefits and shortcomings from the initiation, propagation, and corrosion product accumulation perspectives regarding the use of a corrosion resistant rebar substitution in concrete.

Critical issues specific to the corrosion performance of clad rebar include; determining the "weakest link" that dictates the overall chloride threshold, assessing the effect of clad defect

5

size on corrosion behavior, and verifying the equivalency of clad to solid stainless steel when intact. Since clad stainless steel rebar is significantly cheaper than solid stainless steel rebar, the effect of cladding defects exposing the carbon steel core on corrosion behavior is a critical consideration.

Scope

The corrosion of rebar in concrete can be divided into two stages: An initiation stage and a propagation stage. This project focused on assessing the extension of the initiation stage afforded by novel rebars and characterizing the corrosion propagation stage. The initiation and propagation stages were studied by using lab test methods where the bars could be retrieved following corrosion for examination of the corroded area. In addition to ranking the propagation rate of various alloys, the molar volume of the oxide was compared to the molar volume of the material in the metallic state. Rebars considered in this study are solid 316LN stainless steel, 2101 LDX duplex stainless steel, MMFX-2 steel, carbon steel, and 316L stainless steel clad over carbon steel.

Objective

Therefore, the objectives of this investigation were to assess the corrosion resistance of the newcomers (2101 LDX and MMFX-2), the corrosion propagation characteristics, and the molar volume of oxides compared to the metallic state of all of these new bars. All of this information will enable us to rank all the new bars with respect to (1) the initiation phase, (2) the propagation phase, and (3) the combination of both phases.

MATERIALS AND METHODS

Corrosion Resistant Rebar Candidates Used in This Study: Composition and Metallography

316LN stainless steel, 2101 LDX duplex stainless steel, MMFX-2, solid carbon steel, and 316L clad stainless steel over carbon steel were investigated. Rebar compositions and UNS numbers are presented in Table 1.

General corrosion behavior metrics based solely on the composition including PREN (Pitting Resistance Equivalent Number), CPT (Critical Pitting Temperature, and CCT (Critical Crevice Temperature) are presented in Table 2. The PREN, CPT, and CCT are empirical equations used to express the localized corrosion resistance of an alloy based on composition given by *eqn. 1* (PREN)*, eqn. 2* (CPT)*, and eqn 3* (CCT) (Renner et al., 1986; Sedriks, 1996):

$$PREN = \%Cr + 3.3\%Mo + 30\%N \qquad (eqn.\ 1)$$

$$CPT(C^o) = 2.5\%Cr + 7.6\%Mo + 31.9\%N - 41 \qquad (eqn.\ 2)$$

$$CCT(C^o) = 3.2\%Cr + 7.6\%Mo + 10.5\%N - 81 \qquad (eqn.\ 3)$$

The PREN predicts the relative resistance to localized corrosion for each rebar type while the CPT and CCT more specifically predict the critical temperature below which an alloy is immune to pitting corrosion and crevice corrosion, respectively. All bars were size #5 (diameter ≈ 16 mm) with the exception of 316L clad stainless steel bar, which was size #6 (diameter ≈ 19 mm, with a 1-3 mm thick clad layer over a carbon steel core).

Table 1. Compositions (wt.%) and UNS Numbers

Rebar	C	P	S	Mn	Si	Cr	Ni	Mo	Cu	N
Carbon Steel (ASTM A615)	0.440	0.010	0.029	1.260	0.230	0.150	0.097	0.018	0.280	0.012
Clad Layer (UNS S31603)	0.044	0.031	0.001	1.330	0.390	16.710	10.160	2.700	0.360	0.038
MMFX-2 (UNS *NA*)	0.074	0.007	0.011	0.460	0.230	9.310	0.089	0.023	0.100	0.013
2101 LDX (UNS S32101)	0.030	0.014	0.002	4.750	0.720	21.220	1.580	0.290	0.330	0.226
316LN (UNS S31653)	0.030	0.019	0.015	1.550	0.420	17.790	11.590	2.780	0.240	0.213

Table 2. PREN, CPT, and CCT of candidate rebar materials used in this study

Rebar Type	PREN	CPT ($^\cdot$C)	CCT ($^\cdot$C)
Carbon Steel (ASTM A615)	0.56	-40.11	-80.26
Clad Layer (UNS S31603)	26.76	22.51	-6.61
MMFX-2 (UNS *NA*)	9.78	-17.13	-50.89
2101 LDX (UNS S32101)	28.96	21.46	-8.52
316LN (UNS S31653)	33.34	31.38	-0.71

Surface Condition

The effect of rebar surface condition on corrosion initiation was investigated by testing rebar materials with and without mill scale. Stainless steel manufacturers recommend mill-scale removal but mill-scale non-removal remains a tempting economic consideration. The issue originates from the treatment of the rebar after it has been rolled, which determines the surface condition. The bars develop a thick oxide (mill or furnace scale) following heat treating during processing, typically conducted in the temperature range of 800 to 1100 ($^\cdot$C). The oxide, which forms at high temperature, depletes chromium from the alloy and thus produces an outer layer with lower corrosion resistance than the parent metal (Li et al, 2004). The passivity afforded by chromium on stainless steel is lost in the outer layers of the rebar alloy. Moreover, formation of a less adherent and possibly anion selective oxide layer exposes a chromium depleted steel surface (Stott and Wei, 1989). Because of the loss of corrosion resistance on outer surface layers, most final stainless steel products used in other applications receive a pickling or acid wash to remove the thermal oxide and facilitate formation of a stable chromium-containing

passive oxide layer to maximize corrosion resistance (ASTM standard A380). All rebars used in this study, with the exception of solid 316LN stainless steel and 316L Clad, were received with an existing mill scale. The solid 316LN and 316L clad rebar received a pickling treatment prior to shipment from the manufacturer. Consequently, the 316LN was tested in both the pickled state and after heat treating at 1050°C for 1 hour and air cooling, in order to produce a high temperature oxide similar to a mill scale formed during final solution annealing. Likewise, pickling on 2101 LDX, MMFX-2, and carbon steel was performed according to the ASTM standard A380 – 99e1, using an aqueous solution of nitric and hydrofluoric acid at 60º C for approximately 5 (MMFX-2 and carbon steel) and 30 (2101 LDX) minutes, depending on the intrinsic corrosion resistance of the material. Intermittent wire brush scrubbing was performed to facilitate removal of the mill scale in order to passivate the surface; see Figure 2.
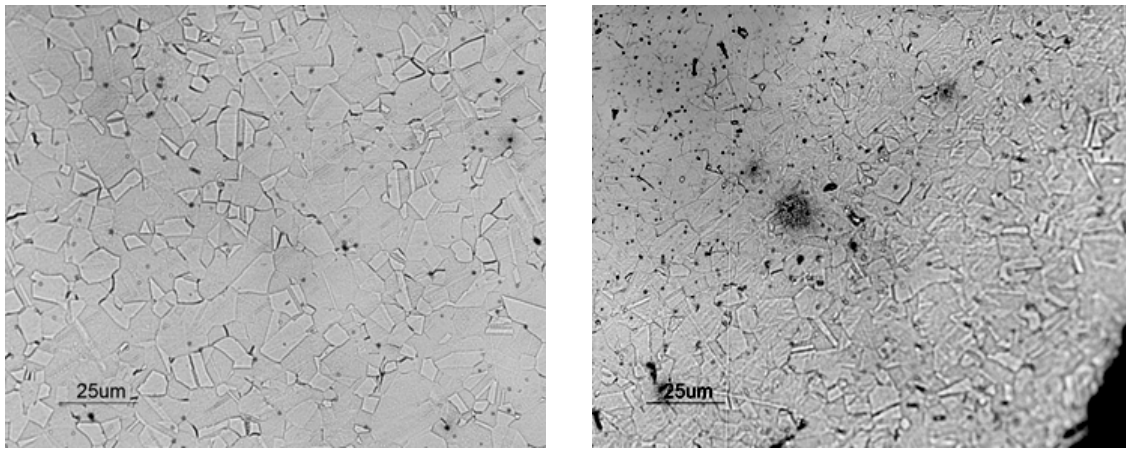
316LN Solid Stainless Steel

316LN is a single-phase austenitic stainless steel, similar to 316L with additional Nitrogen added. In general, 316LN has very similar materials properties compared to 316L, however the increased Nitrogen gives it a higher yield strength and improved corrosion resistance (as seen in *eqn. 1*). The 316LN rebar was produced is accordance with ASTM A955 governing the standard mechanical property requirements for stainless steel rebar, and exceeds the standards for strength and ductility. 316LN is however the most expensive of the bars considered and the estimated initial cost to implement is four to six times more than that of carbon steel. Metallography was performed (for all rebar samples) after polishing the transverse face to 0.05 μm Alumina and etching with Kellers etch (1:1:1, $HCl:HNO_3:H_2O$). Metallographic images revealed a homogeneous, fine-grained austenitic microstructure with randomly spaced inclusions (Figure 3). The outer ~75 μm displayed somewhat smaller grains compared to the center (Figure 3).
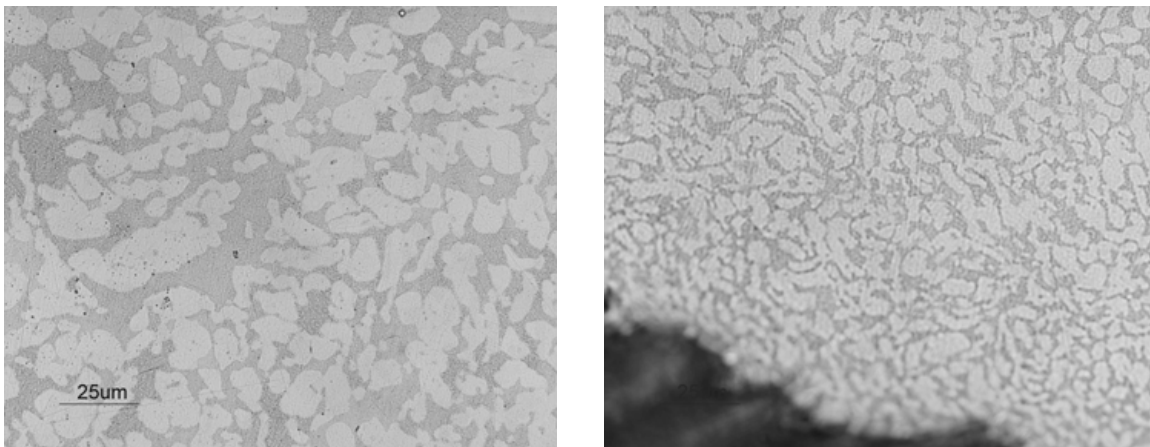
2101 LDX Duplex Stainless Steel

2101 LDX is considered a low-alloy duplex stainless steel mainly because of the relatively low concentration of Ni and Mo (1.58 and 0.29 wt %) compared to conventional austenitic stainless steels. The microstructure of 2101 contains relatively equal parts of austenite and ferrite, with smaller grain structure observed to the outer edge of the rebar sample (Figure 4). No discernable difference in the composition of the two phases was seen (up to the limits of detection) through EDS characterization on the SEM, confirming a balanced composition between the phases. Duplex steels are more susceptible to the formation of phases, such as σ phase, which are detrimental to the corrosion resistance and ductility of the material (Sedriks, 1996). Sigma phase forms slowly between 700˚C and 900˚C and is avoided by controlling the cooling rate during processing (Sedriks, 1996). The 2101 rebar sample was tested to reveal the presence of any detrimental phase (such as σ or χ) formation according to ASTM A923-01. The micrograph of etched 2101, shown in Figure 5, reveals some preferential attack at the grain boundaries, seen by the small black dots near boundaries. These areas may be initial sites of sigma phase precipitation during early growth. Figure 5 was not representative of the entire sample and the preferential attack at the grain boundaries was seen in only a few discrete areas. Moreover, since the areas of preferential attack (small black dots) can be seen in both phases, the presence of sigma phase was not confirmed.

8

Figure 2. The surface appearance of 2101 duplex stainless steel (left) and MMFX-2 (right) in the as-received condition and with the mill scale removed by pickling in a hot nitric and hydrofluoric acid bath.

Figure 3. Optical micrographs of the microstructure of 316LN stainless steel rebar from the center (left) and edge (right) of the polished transverse face with exterior surface in lower right. Samples were etched in HCl + HNO$_3$ solution.

Figure 4. Optical micrographs of the microstructure of 2101 LDX duplex stainless steel rebar from the center (left) and edge (right) of the polished transverse face with exterior surface in lower left. Samples were etched in HCl + HNO$_3$ solution. Light and dark regions indicate ferrite and austenite phases.

MMFX-2 Rebar

MMFX-2 rebar contains 9.3% Cr and is produced through a proprietary production process which claims to form a martensitic microcomposite structure (MMFX product bulletin, 2001). An example of the grain structure can be seen in Figure 6. Although not visible at the resolution of the micrograph presented, MMFX product literature states that "the designed microstructure consists of untransformed nano sheets of austenite between laths of dislocated martensite (MMFX product bulletin, 2001)."

The intent of the MMFX-2 processing technique is to reduce drastically the amount of carbides, which are cathodic to the matrix. The logic behind this is that general corrosion requires anodes and cathodes, and that elimination of cathodes reduces corrosion susceptibility. However, responsive anodes remain present. Ideally, the MMFX-2 provides a microstructure that increases the corrosion resistance while keeping the cost low relative to solid stainless steel. However, despite the elimination of carbides the PREN remains low; PREN = 9.8 (Table 2), which suggests that the resistance to local corrosion will still be poor.

Carbon Steel Rebar

Conventional carbon steel rebar was included to provide a baseline for comparing the candidate corrosion resistant rebar types.   The microstructure is typical for slow-cooled hypoeutectoid steel, with a ferrite-pearlite structure (Figure 7). The outer edge of the transverse cross section contains a higher fraction of pearlite, likely due to a faster cooling rate compared to the middle of the rebar allowing less time for ferrite growth (Figure 7). The PREN for carbon steel is very low (PREN = 0.56) due to a lack of alloying elements, indicating a low intrinsic resistance to pitting or crevice corrosion.

316L Clad over Carbon Steel Rebar

Theoretically, stainless clad rebar posses all the benefits of solid stainless steel bar at half the cost. The clad bars were produced by packing 316L stainless steel pipes with fine granules of carbon steel (wt% C = 0.33). The composite pipes, with carbon steel packed interiors, were then heated to 1250˚C and hot rolled to the appropriate dimensions with standard exterior rebar ribs. The stainless steel cladding thickness was ~1-3 mm and provides durable and economical protection of the carbon steel core (Figure 8). Metallography of the carbon steel core revealed a similar microstructure to that of solid carbon steel rebar with the exceptions that the grain size was noticeably smaller and there was a slightly larger fraction of ferrite compared to pearlite (Figure 9). The 316L clad layer possessed a microstructure very similar to that of the solid 316LN stainless steel rebar shown in Figure 9. The interface lacked porosity (Figure 10).
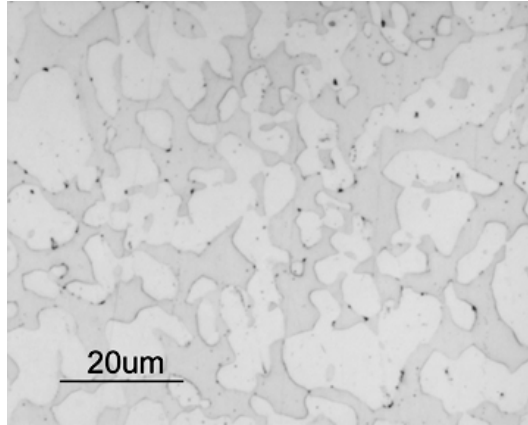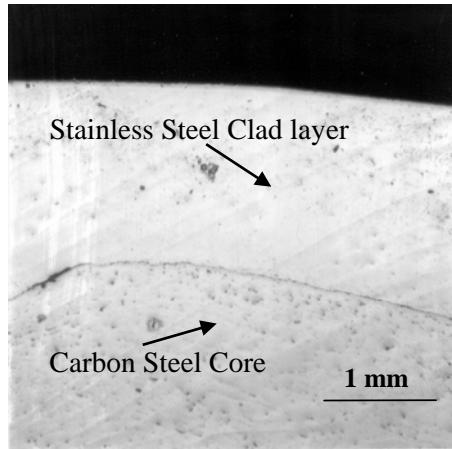
Figure 5. Optical micrograph of the microstructure of 2101 LDX duplex stainless steel, etched according to ASTM A923, in order to reveal the possible presence of sigma phase. Sample was etched in NaOH solution. Black spots indicate possible sites for sigma phase (unconfirmed).
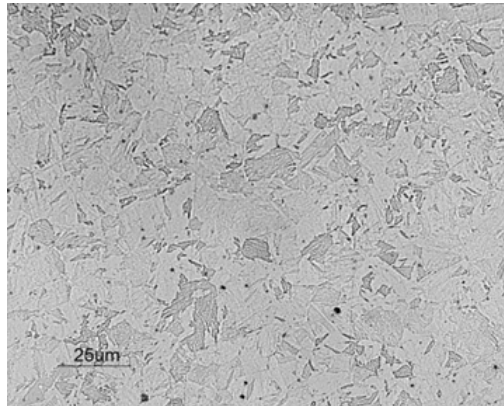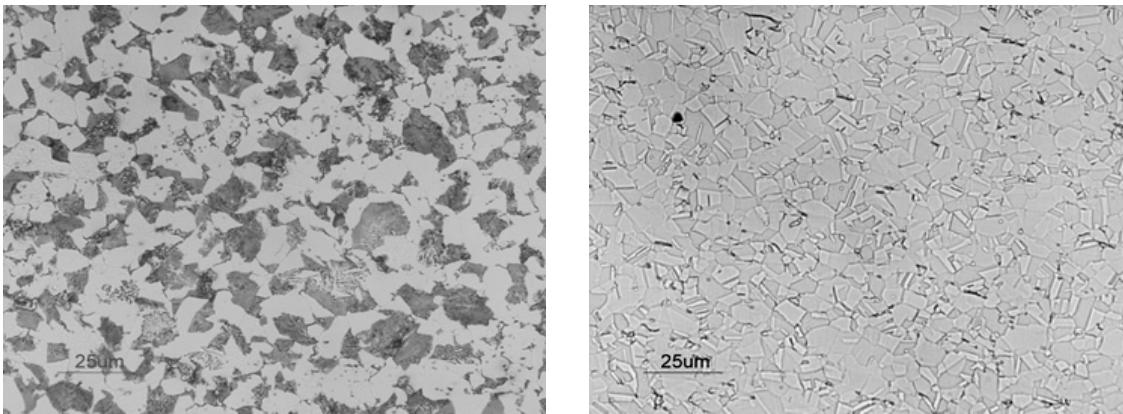

Figure 6. Optical micrograph of the microstructure of MMFX-2 rebar from the polished transverse face. Sample was etched in HCl + HNO$_3$ solution. The microstructure shown is and Fe-Cr solid solution containing prior autensite boundaries and a lath structure.
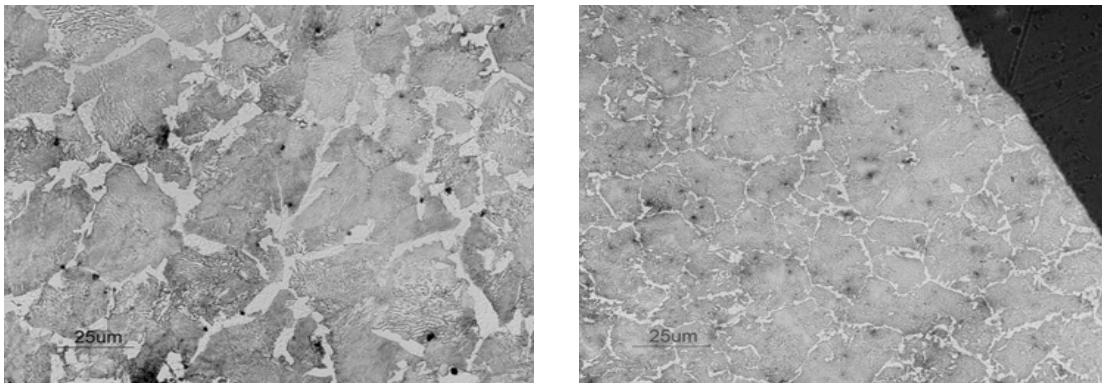

Figure 7. Optical micrographs of the microstructure of conventional carbon steel rebar from the center (left) and edge (right) of the polished transverse face with exterior surface in upper right. Samples were etched in HCl + HNO$_3$ solution. Dark regions show the pearlite eutectoid structure while light regions show the proeutectoid ferrite phase

11

Figure 8. Partial view of a cut end (cut transverse to the bar length) of 316L stainless steel clad rebar, showing the cladding thickness.

Figure 9. Optical micrographs of the microstructure of 316L clad rebar from the polished transverse face of the carbon steel center (left) and 316L stainless steel clad layer (right). Samples were etched in HCl + HNO$_3$ solution. The carbon steel core contains dark regions of pearlite and lighter areas of ferrite while the stainless steel structure is that of single-phase Fe-Ni-Cr solid solution.
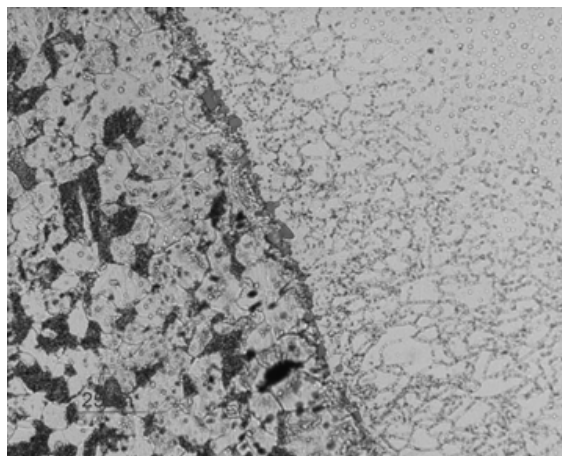
Figure 10. Optical micrograph of the clad layer/core interface of 316L stainless steel clad (right side) over carbon steel core (left side) rebar.

However, the lack of nitrogen in the clad layer creates a lower PREN than seen for solid 316LN. The 316L stainless steel clad/carbon steel core interface is shown in Figure 10. Figure 10 reveals that excellent bonding was achieved between the clad layer and the core, and the interface was free of large voids. The etching was adequate to reveal the microstructural features of both materials. It is likely that the dark areas of attack at the interface were due to carbon segregation to the interface. Furthermore, the stainless steel clad layer showed a more heavily etched microstructure starting at the interface and extending ~50 µm into the clad layer, which can be explained by possible diffusion of carbon from the carbon steel core into the inner surface of the cladding during heating and hot rolling. This may affect the corrosion resistance but the outer portion was free of this type of carbon ingress.

METHODS

Experimental Setup

Resistance to initiation was investigated through the determination of chloride threshold levels associated with potentiostatic current detection in a simulated synthetic pore solution. Experiments performed in a standard three-electrode electrochemical configuration. Electrochemical testing was performed in two types of electrochemical cells (Hurley et al., 2001). One enabled standard mounting and testing of a flat polished metallic surface. The other was a custom-built electrochemical cell that enabled testing of the original surface of the rebar in a vertical orientation. Local corrosion was investigated without intentional artificial crevice formers. However, the experimental set-up did not exclude naturally occurring occluded geometries (e.g., the roughness of the sample in the as-received or pickled condition and possible inherent micro-crevices especially along the ribbing of the rebar).

Rebar samples were cut to expose cross sections, spot welded with a nickel ribbon on the unexposed face, and set in mounting epoxy. The rebar sample (cross-section face) was wet polished through 800 grit SiC paper, degreased with acetone, rinsed with deionized water, and air dried. Clad rebar cross-sections were not tested in this manner. Vertical cell test samples were prepared from $\approx$ 70 mm and $\approx$ 35 mm sections of rebar. One end of each test piece was drilled and tapped with $\approx$ 40 mm piece of 1040 threaded rod, shown in Figure 11. This established electrical contact with the sample and served as a sample holder when threaded with a No. 3 rubber stopper. Copper paste was added at the threaded interface between the threaded rod and the rebar to enhance electrical contact. The threaded rod was secured to the rebar with a stainless steel hex nut, with all mounting attachments above the water line. Additionally, the hex nut and the tapped end of the sample were covered with an anti-crevice mask to prevent electrolyte contact and unwanted secondary electrochemical reactions (Figure 11). The vertical cell enabled testing of the rebar surface that was exposed during service as well as a cut cross section. Both pickled and mill scale conditions were investigated. Prior to testing, each rebar specimen was washed, degreased and ultrasonically cleaned in acetone, rinsed with deionized water, dried at room temperature, and stored in a vacuum jar. Separate from the standard rebar geometries tested, a few 316L stainless steel clad bars were bent in a "U" shaped bend configuration. In this configuration, the clad rebar was tested without exposing the carbon steel core or a cap at the cut end.

13

Propagation experiments were performed in the flat cell utilizing a standard three-electrode electrochemical cell configuration in saturated $Ca(OH)_2$ + NaCl ([Cl$^-$] near [Cl$^-$]$_{threshold}$ for each material, Table 3). Rebar samples were cut to expose cross sections, spot welded with a nickel ribbon on the unexposed face, and set in mounting epoxy. The rebar sample (cross-section face) was wet polished through 800-grit SiC paper, degreased with acetone, rinsed with deionized water, and air-dried. Further, in order to control the anode area exposed, the electrode surface was masked with electroplaters tape to expose a circular area of approximately 0.5 mm^2.
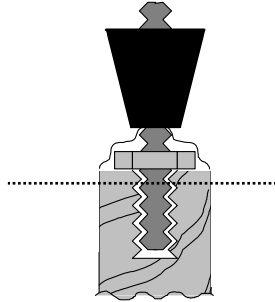
Figure 11. Cross-section schematic view of the top of a rebar sample designed for chloride threshold testing in a vertical test cell.

Electrochemical Testing

Test Environments

Saturated $Ca(OH)_2$ was used to simulate the concrete environment. Chloride was added to facilitate consistent initiation of stable active corrosion. The critical chloride concentration required to cause local corrosion is known as the chloride threshold (chloride) concentration. Synthetic pore solution tests have been used elsewhere for simulating the concrete environment (Alonso et al., 2000; Li and Sagüés, 2001). Synthetic pore solution yields less spread in the chloride threshold data for plain carbon steel bars, possibly by the elimination of many variables associated with the concrete matrix and the concrete/rebar interface (Hurley and Scully, 2002). Greater control is gained over the Cl$^-$ to OH$^-$ ratio. Moreover, it has been found that the chloride thresholds from simulated pore solution tests are more conservative than in concrete tests (Yonezawa et al., 1998). $Ca(OH)_2$ + NaCl solutions are used in the present study in initiation tests.

The large differences in resistance to corrosion for each rebar material (established via chloride threshold determination) required different chloride concentrations to be used during similar corrosion propagation tests, depending on the corrosion initiation behavior specific to each material. Table 3 summarizes the test environments used during radial, lateral, and pitting factor corrosion propagation tests.

Table 3. A summary of the testing environments used during various corrosion propagation characterization experiments.

Test Type	Carbon Steel	316LN	2101	MMFX-2
Radial Propagation	Sat. Ca(OH)$_2$ + 0.1 M NaCl	Sat. Ca(OH)$_2$ + 2 M NaCl	Sat. Ca(OH)$_2$ + 1 M NaCl	Sat. Ca(OH)$_2$ + 0.1 M NaCl
Lateral Propagation	Sat. Ca(OH)$_2$ + 0.2 M NaCl[‡]	3 M NaCl (pH 7)[†]	--	--
	w/ Sand + Glass Beads added	w/ Sand + Glass Beads added		
Pitting Factor	Sat. Ca(OH)$_2$ + 0.1 M NaCl	Sat. Ca(OH)$_2$ + 2 M NaCl	Sat. Ca(OH)$_2$ + 1 M NaCl	Sat. Ca(OH)$_2$ + 0.1 M NaCl

[‡] **Simulated defective clad was also tested in this solution.**
[†] **The electrolyte used in 316L testing was aqueous NaCl, without saturated Ca(OH)$_2$.**

In some lateral propagation tests, sand and glass beads were added to the electrolyte in order to simulate non-conductive aggregate of similar size found in actual concrete. The addition of sand and glass beads provides possible crevice initiation sites when in contact with the electrode surface and has a small effect on ionic transport (Hurley, 2002).

Potentiostatic Testing to Determine Threshold Chloride Level: Incremental and Fixed Chloride Concentration

Potentiostatic testing was carried out at +200 mV (vs. SCE) in saturated Ca(OH)$_2$, with chloride levels adjusted using NaCl. Two variations of potentiostatic tests were performed: incremental chloride additions and using constant chloride concentrations. For the incremental chloride addition tests, chloride additions were made every 24 hours following an initial 24-hour period without chloride, until the cut off anodic current density of 1-2 μA/cm^2 was exceeded, associated with onset of passivity breakdown and active corrosion. Upon reaching the threshold current density, the test was terminated. The threshold chloride content was noted as the cumulative amount of chloride that had been added throughout the duration of the test. Chloride additions were made every 24 hours in order to give the system sufficient time to stabilize at each concentration. Constant chloride concentration tests were also performed at +200 mV vs. SCE for 24 hours. These tests were conducted using separate rebar samples and NaCl + saturated Ca(OH)$_2$ solutions over a range of chloride concentrations. Active corrosion was detected by an increase in current density above 1-2 μA/cm^2.

Constant chloride concentration experiments were conducted to enable the control of testing duration. In contrast, the duration of incremental chloride addition tests was governed by the chloride step size chosen. The relatively large differences in corrosion resistance of rebar materials with different compositions made using a uniform chloride increment for all tests difficult due to excessive test duration (with a small uniform increment) or poor chloride threshold resolution (with a large chloride increment). The issue becomes more complicated if the chloride threshold is dependent on test exposure duration. The constant chloride concentration test is less realistic, since in reality it takes many years for sufficient chlorides to

accumulate at the rebar interface. However, the constant chloride method enables better resolution of the chloride threshold for breakdown of passivity for vastly different rebar materials at identical test durations.

Effect of Sample Aging on Threshold Chloride Level

The test duration prior to corrosion initiation may influence the obtained chloride threshold values due to maturing of the passive film. The passive film will continue to evolve throughout the lifetime of a concrete structure as the outer layer of the oxide continues to react with the surrounding environment (Bentur et al., 1997; Olsson and Landolt, 2003). The passive film growth kinetics are nearly identical for Fe and 304L stainless steel in alkaline solution (Borate buffer pH = 8.4) (Davenport and Lee, 2002) . Moreover, the passive film for rebar in concrete forms in two layers: a tightly adhering inner layer of Fe_3O_4 (Cr_2O_3 for stainless steel) and an outer layer of poorly crystallized Fe^{2+}/Fe^{3+} hydroxide on both carbon steel and stainless steel rebar (Veleva et al., 2002). Studies on stainless steel have shown that passive film growth occurs in a matter of minutes, while long range annealing of the passive film structure is considerably longer and begins to slow after several hours (Olsson and Landolt, 2003; Veleva et al., 2005). Additionally, AES (Auger Electron Spectroscopy) on carbon steel demonstrated that no significant further evolution in the thickness or O/Fe ratio of the passive film occurs as the samples are aged from 1 week to 1 month at OCP in cement pore solution (Montemor et al., 1998). These results suggest that the bulk of the oxide thickening process occurs in the first few days of exposure. However, aging involving defect annealing and the continued, relatively slow, oxidation of Fe^{2+} to Fe^{3+} in the outer layer of the oxide continues for the entire duration that a sample is aged. For actual rebar in concrete, the aging process will continue for many years as long as the rebar remains in a passive state. An effort was made to artificially age chloride threshold samples to simulate long-term aging conditions for concrete. In order to characterize the degree of aging, EIS was conducted in the flat cell on 316LN samples polished to 1200 grit and artificially aged at both +200 mV vs. SCE and at OCP, for various exposure times. EIS scans were conducted at applied AC frequencies from $1x10^5$ to $1x10^{-4}$ Hz, at OCP. The goal of these experiments is to determine artificial aging conditions that simulate long term OCP aging, via comparison of the resultant R_p values. From the EIS results and data previously published by other authors, vertical cell rebar samples were aged at +200 mV vs. SCE for 3 days in saturated $Ca(OH)_2$ in order to form a passive film that simulates long-term natural aging of the passive film. Following artificial aging, the chloride threshold was determined via constant chloride concentration potentiostatic testing. Aging samples for 3 days at +200 mV vs. SCE in non-chloride solutions was chosen to provide sufficient accelerated aging and for convenience of comparing the resulting chloride threshold values. Recall that previous chloride threshold testing was conducted at +200 mV. Under these conditions, the nature of the passive layer is comparable to aging in concrete for at least 2 years.

Radial Propagation

The characteristic propagation rate per defined unit area of each new bar was established by recording the anodic current at potentiostatically-applied potentials (e.g., infinite cathode) from anode sites of known area. Corrosion damage was initiated and propagated at an elevated potential relative to the open circuit potential, on a sample with approximately 0.5 mm^2 of exposed area. This established an active corrosion environment in a controlled damage volume

that can be quantitatively characterized (as opposed to a planar electrode with multiple uncontrolled initiation sites). Following the initial propagation stage where a local corrosion site was grown over the entire anode, the potential was stepped down and the current response monitored. Radial propagation was considered stopped when the current decreased significantly to indicate repassivation or switched signs and began to increase (at low potentials) indicating that the sample had become cathodically polarized. An approximated damage volume enables assessment of the radial penetration rate as a function of potential and time through Faraday's law, for the rebar compositions investigated. The corrosion current (I) behavior given by the function in *eqn. 4* was determined versus time from experimental data to establish $I^*(E_{applied})$ at each potential step as a function of time (t^n).

$$I(E_{applied}, t) = I^*(E_{applied})t^n \qquad (eqn.\ 4)$$

The radial corrosion attack depth r was then expressed as the volume of a growing hemisphere *(eqn. 5)*.

$$r = \left[\frac{Q \cdot E.W.}{(\frac{2}{3}\pi)\rho F} \right]^{1/3} = \left[\frac{I^*(E_{applied})E.W.}{(\frac{2}{3}\pi)\rho F(n+1)} \right]^{1/3} \cdot t^{\frac{n+1}{3}} = kt^{\frac{n+1}{3}} \qquad (eqn.\ 5)$$

Where E.W. is the alloy equivalent weight, ρ is the alloy density, F is Faraday's constant, t is time and n is an integer. To analyze the corrosion penetration behavior it is useful to consider the change in corrosion penetration depth (r) with each potential step following corrosion initiation assuming hemispherical damage volume. Other geometries may be used to describe the damage volume, such as a cylinder or hemispheroid, depending on the actual damage geometry. The assumption of hemispherical pit growth has been validated in the literature for single pits allowed to grow on aluminum and stainless steel in 3-D (i.e., not a 1-D wire electrode with inert side walls or a 2-D sheet electrode with an inert base) (Hunkler and Bohni, 1981; Newman and Franz, 1984; Wong and Alkire, 1990). r vs. t can be plotted by first determining the incremental r from $I(E_{applied},t)$ versus time data at each potential using *eqn. 5*. Here, corrosion penetration rate data may be analyzed assuming that active pit depth growth follows a power law model such that $r = kt^{(n+1)/3}$, where r is the hemisphere radius (cm), t is time, and k is constant dependent on potential. In this case, the constant k can be directly calculated using known rebar alloy materials properties and the relevant electrochemical dissolution data via *eqn. 5*. Therefore, the radial corrosion propagation rate is dependent on the physical properties of the rebar material *(ρ, E.W.)* and $I(E_{applied}, t)$, which is determined by the materials response to the test environment at a given potential.

Lateral Propagation Using Multiple Micro Electrode Arrays

In an effort to characterize the lateral spreading of corrosion along a metal surface, it is desirable to obtain discrete electrochemical measurements on localized regions as they become active. Coupled close-packed micro-electrode arrays (MEAs) provide a method which enables an array of electrodes to behave as a single global electrode, while the behavior of each micro-electrode can be monitored individually (Budiansky et al., 2004). An MEA consists of a close-packed array of electrically isolated electrodes which are galvanically connected through zero-resistance ammeters (ZRAs) (Budiansky et al., 2006). The array simulates a continuous planar

electrode while still allowing individual current measurements to be made at each microelectrode. Another benefit of MEAs is that specific electrochemical conditions may be prescribed on selected electrodes and the effect on the surrounding electrodes may be monitored. For example, corrosion may be allowed to initiate and spread naturally or it can be preferentially initiated on a group of electrodes by holding them at an elevated potential relative to the rest of the array. Thus, the impact of nearby actively corroding electrodes on surrounding electrodes may be monitored.

A multi-microelectrode assembly of individually addressable electrodes was utilized to investigate the lateral spread of corrosion originating from points of local breakdown. 100 wire (diameter = 250 μm), 5x20 close-packed electrode arrays were built of carbon steel and 316L stainless steel, to compare the difference in corrosion spreading between the materials. Wire used for electrode array construction was insulated with a thin (18 μm) organic coating (polyamide) so that each electrode was electrically isolated preventing unwanted galvanic coupling via wire-to-wire contact. Theoretically, the separation distance between electrodes in an array is 36 μm. Electrode arrays were embedded in epoxy and electrical connections were made by individually soldering each electrode to an insulated wire. Additionally, a third array was constructed with the goal of simulating defective stainless steel clad over carbon steel rebar. This array was designed to replicate the situation in which the stainless steel clad layer has been breeched exposing a relatively small area of carbon steel. The simulated defective clad rebar array (5x20) was constructed with two adjacent 5 electrode columns (col. 9 and 10) of carbon steel in the middle and the remaining electrodes (col. 1-8 and 11-20) 316L stainless steel. MEA testing was conducted in saturated $Ca(OH)_2$ + NaCl and also with sand and glass beads added to simulate possible crevice conditions found in concrete due to non-conducting aggregate in contact with the electrode surface. Samples were first exposed to saturated $Ca(OH)_2$ chloride free electrolyte for an initial period of 10 minutes after which NaCl was added to achieve $[Cl^-] \geq [Cl^-]_{threshold}$. The chloride concentration used in carbon steel and simulated defective clad testing was 0.2 M NaCl while 3 M NaCl was used for 316L stainless steel testing. Experiments were conducted with all electrodes held at 0.2 V vs. SCE ("natural"), considered a conservative long term OCP value for stainless steel in concrete and perhaps an attainable galvanic couple potential when coupled to a large array of passive rebar materials. This allowed natural corrosion initiation and spreading, but not control of initiation sites. Additionally, to observe the effect of corrosion spreading from pre-selected active sites, testing was conducted with the two middle columns of 5 electrodes (5x20 array) held at an elevated potential ("activated columns"), 0.5 V vs. SCE for carbon steel and 1 V for stainless steel, while all other electrodes were held at 0.2 V vs. SCE. Experimental duration was 5 hours unless all electrodes demonstrated stable active corrosion, in which case the test was terminated.

Pitting Factor Analysis to Assess Lateral Propagation

Pitting factors of candidate rebar materials was determined by calculating the mass loss (gravimetrically) and characterizing the morphology of corrosion following electrochemically induced damage. Galvanostatic testing performed at different time durations enables a similar amount of corrosion damage to be specified for each material. Coupons machined from rebar samples yielded test specimens that have equivalent pre-test geometries of approximately 29.3 mm by 12.5 mm by 6.3 mm. Corrosion damage was initiated and propagated galvanostatically at

0.01 Amps for periods of 12, 24, and 48 hours in saturated $Ca(OH)_2$ + NaCl ($[Cl^-] \geq [Cl^-]_{threshold}$; see Table 3).

Post-test analysis following specimen cleaning consisted of mass loss measurements with conversion to average depth of attack via *eqn. 6* and maximum pit depth characterization with the confocal scanning laser microscope (CSLM) to characterize corrosion morphology unique to the rebar composition. A pitting factor specific to the rebar composition, which describes the active corrosion morphology, was then determined by taking the ratio of the maximum pit depth from CSLM to the average corrosion penetration depth (assuming 100% of the surface is undergoing corrosion) *(eqn 7)*, outlined below:

$$\frac{mass\ loss(g)}{surf.\ area(cm^2) \times \rho(\frac{g}{cm^3})} = \mathrm{a}vg.\ depth\ of\ attack\ (cm) \qquad (eqn.\ 6)$$

$$\frac{max.\ depth\ of\ attack\ (cm)}{avg.\ depth\ of\ attack\ (cm)} = pitting\ factor \qquad (eqn.\ 7)$$

Through this analysis, pitting factors were determined for solid 316LN stainless steel, 2101 duplex stainless steel, MMFX-2, and carbon steel. A pitting factor of 1 indicates entirely uniform corrosion, while higher numbers indicate increasingly localized corrosion.

Corrosion Propagation: Oxide Formation and Collection

Anodic dissolution of rebar during corrosion causes the formation of expansive oxides that eventually crack the surrounding concrete. To study the oxides formed on different rebar alloys, corrosion product samples were collected and analyzed. Production of oxides was accomplished by initiating corrosion on carbon steel, MMFX-2, 2101, and 316LN stainless steel rebar samples using the experimental cell setup previously described for chloride threshold testing. Following initiation, corrosion was allowed to propagate for a period of 48 hours. The samples were then removed from the test cell and corrosion products that were loosely adhered to the sample surface were collected by scraping with a rubber-tipped glass rod. The collected corrosion products were then exposed to air for a duration of >5 days to allow for drying. To facilitate analysis via powder x ray diffraction (XRD), the dried corrosion products were crushed into a fine powder and poured into a zero background holder which was in plane with a source-detector sampling angle of $2\theta = 0°$. For XRD measurements a $Cu_{K\alpha}$ X-ray source was used and diffraction measurements were taken continuously during the Bragg diffraction angle range of $2\theta = 20-85°$. To analyze XRD results the obtained scans were compared to diffraction pattern standards of known inorganic oxide and hydroxide compounds to identify the composition and phases present in the collected corrosion products.

RESULTS

Chloride Threshold by Potentiostatic Holds

Potentiostatic experiments were performed at +200 mV vs. SCE to determine the chloride threshold. A summary plot for potentiostatic tests on pickled rebar materials compared to carbon

steel (as-received and pickled) is presented in Figure 12. Results are grouped by material tested and each circular symbol or data point on the X-axis represents a specific test for which results are displayed in the Y direction. Results of both incremental chloride addition and constant chloride testing are presented on the same plot. Data points connected with a line represent chloride levels achieved during a single incremental chloride addition test on a single specimen, while data points with no connecting line represent results from individual constant chloride tests performed at the indicated chloride concentration. Solid or filled data points, regardless of test method, indicate that the test specimen remained passive during the test duration. Chloride concentrations that caused depassivation and sustained active corrosion are represented with an open circular data point.

Effect of Material Composition on Chloride Threshold

Figure 12 presents results on pickled specimens. The lowest threshold chloride concentration for pickled 316LN recorded ($Cl^-/OH^- = 20$) is approximately double that observed for pickled 2101 LDX (high value, $Cl^-/OH^- = 9.7$) and nearly two orders of magnitude higher than that of as-received carbon steel (high value, $Cl^-/OH^- \leq 0.342$). These results are consistent with those previously published under similar experimental conditions where the chloride thresholds for 304, 304L, and 316L were between 4 and 6% Cl^- ($19.5 < Cl^-/OH^- < 29.3$) (Bertolini et al., 1996). However, 316 stainless steel was still passive at up to 10% Cl^- ($Cl^-/OH^- = 48.9$) when the test was terminated (Bertolini et al., 1996). Pickled MMFX-2, exposed in constant chloride tests, produces some improvement over carbon steel. The high-value chloride threshold from incremental tests was near a Cl^-/OH^- ratio of 4.9. Regarding carbon steel, the results obtained during incremental chloride addition testing ($0.25 < Cl^-/OH^- < 0.34$) agree with previously published results of carbon steel in simulated pore solution ($0.25 < Cl^-/OH^- < 0.8$) (Hausmann, 1967; Gouda and Halaka, 1970; Goni and Andrade, 1990; Alonso et al., 2000; Li and Sagüés, 2001). However, the result from the constant chloride experiments at +200 mV was lower, with a Cl^-/OH^- ratio of 0.049. The comparison of pickled bars to as-received carbon steel (Figure 12) is relevant since carbon steel is not pickled prior to placement in concrete while stainless steel bars would likely be pickled by the manufacturer.

Effect of Stainless Steel Cladding on Chloride Threshold: Intact and With Defects

Results from pickled 316L stainless steel clad rebar in different experimental configurations are presented in Figure 13, in comparison to solid pickled 316LN and unpickled carbon steel.

Exposure of the carbon steel core in the clad bar, such as with a hole drilled through the clad layer and with a cut cross-section exposed, drastically reduced the chloride threshold value to that of carbon steel. Moreover, the U-bend with a drilled hole had a chloride threshold (Cl^-/OH^- ratio) of 0.25. Clad bar with a cut end exposed produced a chloride threshold Cl^-/OH^- ratio of 0.73. Intact clad 316L U-bend specimens had a higher chloride threshold (Cl^-/OH^- ratio of 4.9) compared to carbon steel ($0.25 < Cl^-/OH^- < 0.34$) during incremental chloride addition tests. Yet this value (Cl^-/OH^- ratio of 4.9) was still much lower than solid 316LN stainless steel rebar (Cl^-/OH^- ratio of 20). Such a large difference in chloride threshold was surprising even though the PREN for 316L (26.7) is slightly lower than 316LN (33.3). Corrosion often preferentially initiated along the seam of the cladding during intact U-bend tests (Figure 14).
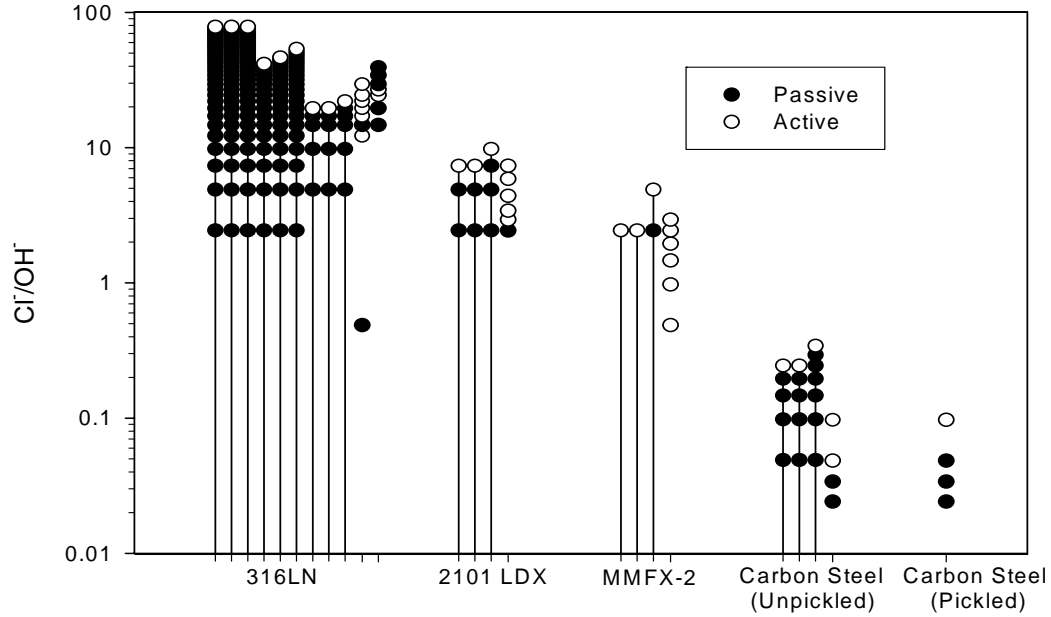
Figure 12. Chloride threshold results obtained from pickled alloyed bars compared to pickled and unpickled carbon steel. Experiments were performed at +200 mV vs. SCE in saturated Ca(OH)$_2$ with various amounts of NaCl added. A line connecting data points indicates incremental chloride concentration testing while data points (with no line) indicate results from constant chloride concentration testing.
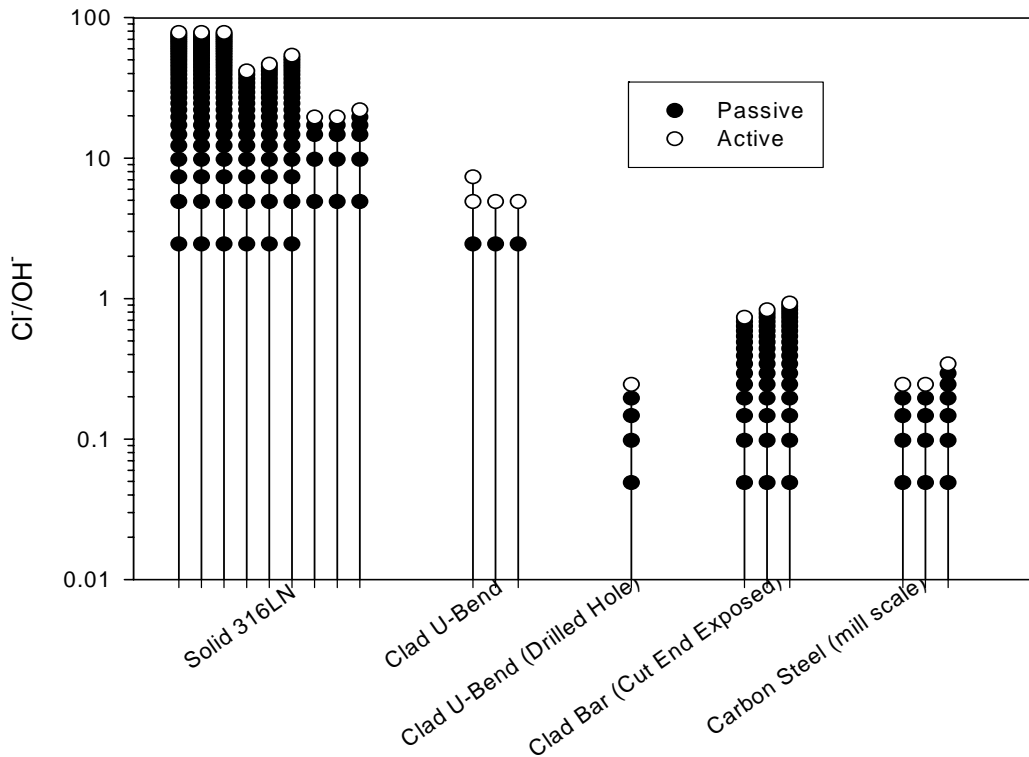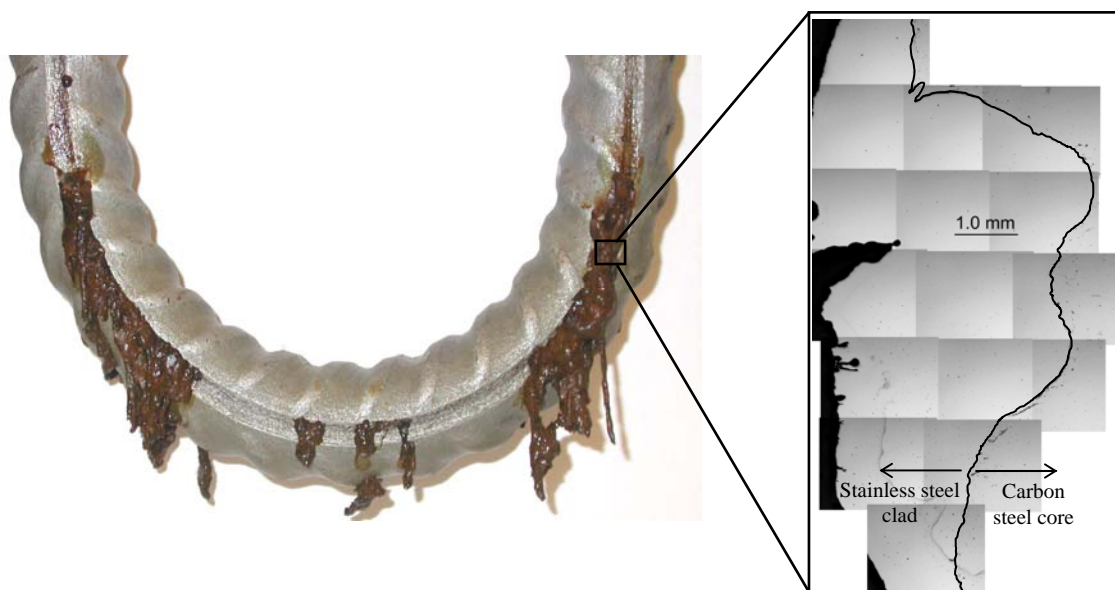

Figure 13. Chloride threshold results obtained from pickled 316L clad and solid 316LN compared to carbon steel rebar during incremental chloride addition testing. Experiments were performed at +200 mV vs. SCE in saturated Ca(OH)$_2$ with various amounts of NaCl added.

21

Figure 14. Post-testing photo from a potentiostatic incremental chloride addition test performed on 316L clad U-bend rebar (see Figure 13). Corrosion initiated preferentially along the cladding seam and had a chloride threshold much lower than solid 316LN rebar. A zoom in of the polished cross section of the seam is shown at right, the clad/core interface has been enhanced with a black line.

Effect of Surface Condition on the Chloride Threshold

The presence of mill scale affected the chloride threshold. All materials tested with mill scale present exhibited a chloride threshold similar to carbon steel (Figure 15). In other words, the presence of mill scale negated any benefit of alloying for corrosion resistance in the test methods used here. A large decrease in chloride threshold concentration with mill scale was seen for both 2101 LDX and 316LN (Figures 16 and 17). 2101 dropped from a Cl^-/OH^- ratio of 2.5 (pickled) to a Cl^-/OH^- ratio of 0.34 (mill scale) during constant chloride concentration tests. 316LN had a drop in chloride threshold with surface condition from a Cl^-/OH^- ratio of 24.5 (pickled) to a Cl^-/OH^- ratio of 0.49 (mill scale) during constant chloride addition tests. A slight improvement with pickling was seen for MMFX-2 as one incremental chloride addition test had a chloride threshold Cl^-/OH^- ratio of 4.88 compared to a Cl^-/OH^- ratio of 0.2 for MMFX-2 with mill scale (Figure 12). In all other tests, MMFX-2 (pickled and with mill scale) behaved similarly to carbon steel; see Figures 12 and 15. The effect of mill scale on carbon steel, as shown in Figure 12, is small when compared to the effect seen for the highly alloyed rebar materials. The effect of mill scale on the chloride threshold for carbon steel has also been shown to be negligible (Mammoliti et al., 1996; Alonso et al., 2000; Li and Sagüés, 2001) and there was no significant difference between the chloride thresholds for ribbed and smoothed plain carbon steel rebars (Alonso et al., 2000). A slight increase was reported for sandblasted ($Cl^-/OH^- = 0.6$) compared to as-received plain carbon bars ($Cl^-/OH^- = 0.3$) in saturated $Ca(OH)_2$, but these results are comparable to the values presented in Figure 12 (Li and Sagüés, 2001). Conversely, a slightly higher chloride threshold was reported for deformed bars (as-received) over smooth bars (mechanically removed ribs and mill scale) although the values reported are higher compared to

values presented here, due to the addition of an 0.1 wt% $Ca(NO_2)$ inhibitor to saturated $Ca(OH)_2$ (Mammoliti et al., 1996). For comparison, the chloride threshold of 316LN is decreased by a factor of ≈100 with mill-scale. It is reduced by a factor of ≈10 for 2101 LDX when mill scale is present. In fact, the higher the PREN number of the candidate rebar material, the more severe the decrease in chloride threshold concentration (Figure 18).

Effect of Test Duration Prior to Introduction of Chloride

Further examination of the data presented in Figure 12 reveals that chloride threshold concentrations obtained from incremental chloride addition tests are generally greater than results obtained from constant chloride tests performed on the same material. Incremental chloride addition tests begin with a period of 24 hours of polarization at +200 mV vs. SCE prior to chloride addition. In comparison, constant chloride tests are exposed to the prescribed chloride level the instant the test begins and polarization to +200 mV vs. SCE commences. The chloride threshold obtained for carbon steel during constant chloride testing with minimal aging was $Cl^-/OH^- = 0.049$, compared to a low value of $Cl^-/OH^- = 0.245$ obtained during incremental chloride testing with substantial aging. Furthermore, incremental chloride addition testing on 316LN conducted with larger chloride increments and therefore shorter test durations resulted in a lower chloride concentration required to cause active corrosion, as summarized in Figure 12. These results indicate that the duration of $Ca(OH)_2$ exposure at +200 mV vs. SCE prior to introduction of soluble chloride has an effect on the chloride threshold value obtained.
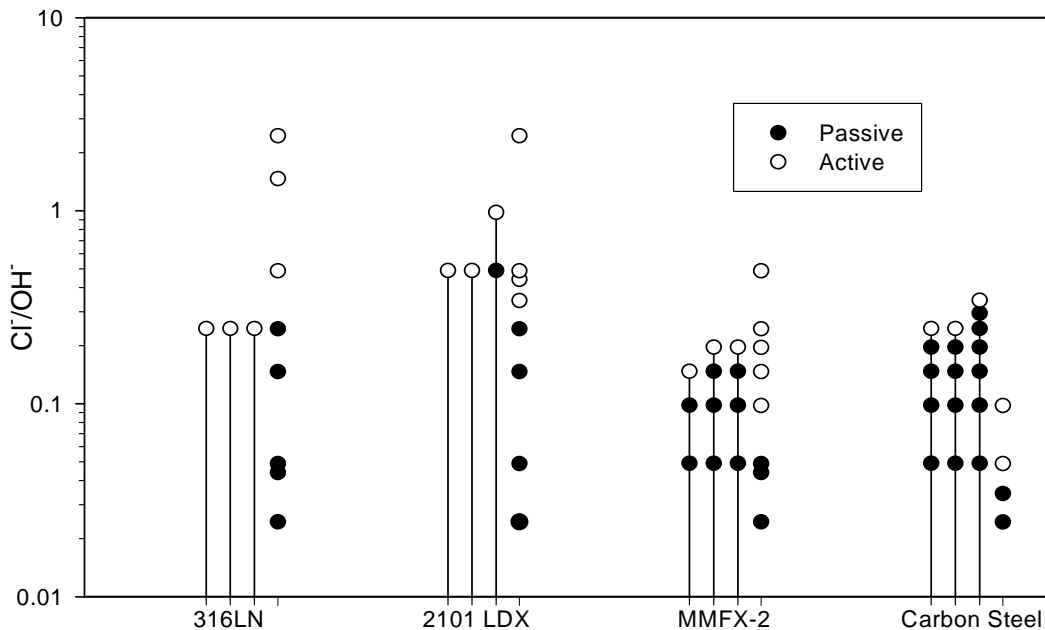
Figure 15.   Chloride threshold results obtained from rebars with mill scale present during incremental chloride addition and constant chloride potentiostatic testing. Experiments were performed at +200 mV vs. SCE in saturated $Ca(OH)_2$ with various amounts of NaCl added.

Figure 16. Chloride threshold results obtained from 2101 compared to carbon steel during incremental chloride addition and constant chloride potentiostatic testing. All samples held at +200 mV vs. SCE in saturated Ca(OH)$_2$ with various amounts of NaCl added.
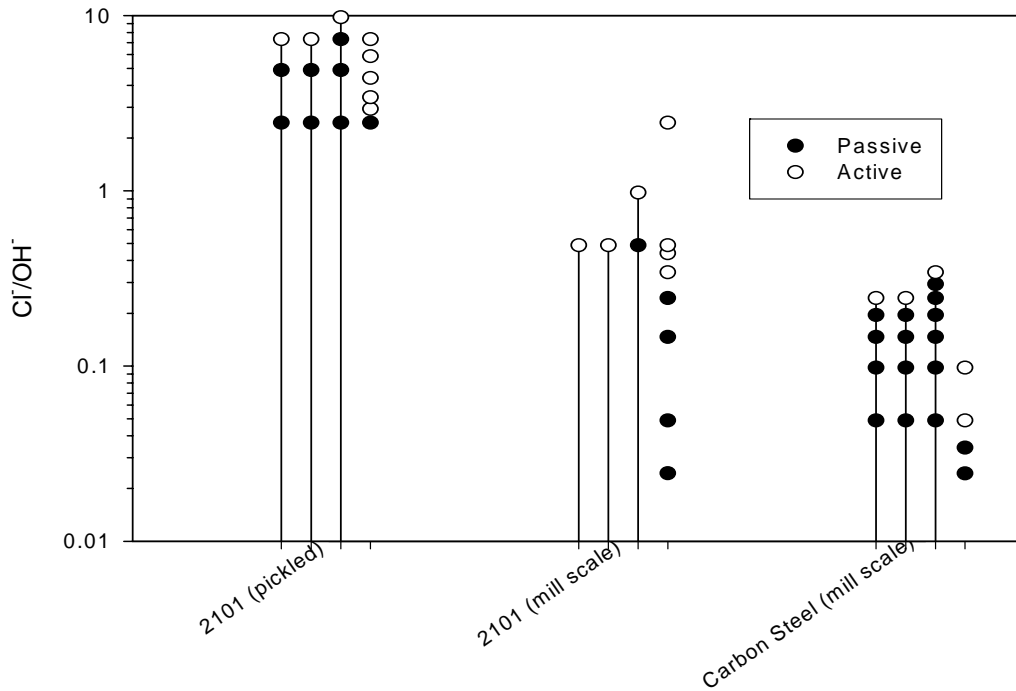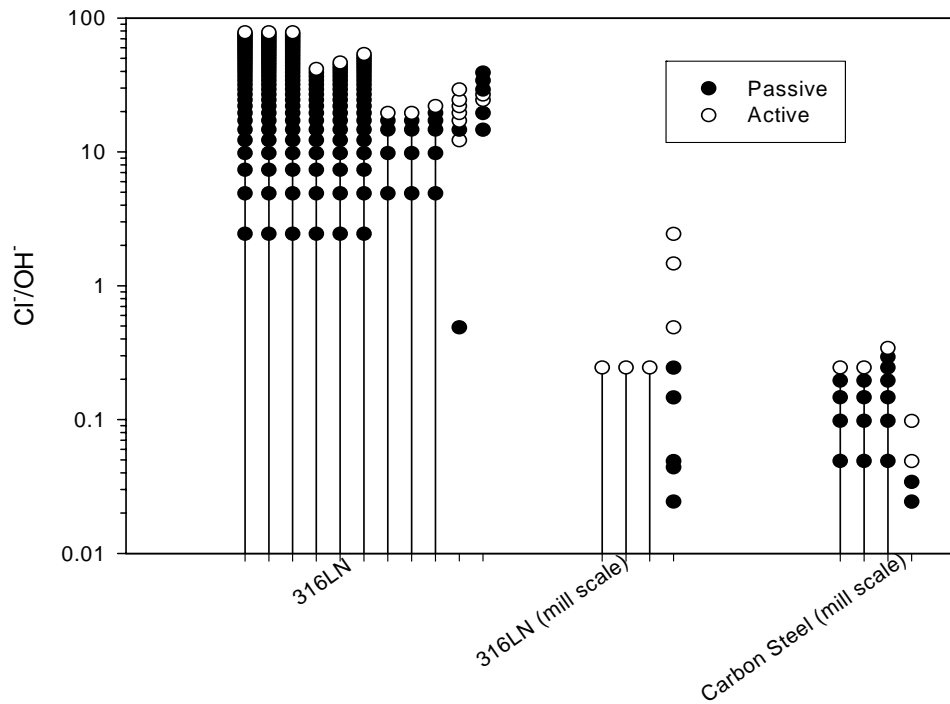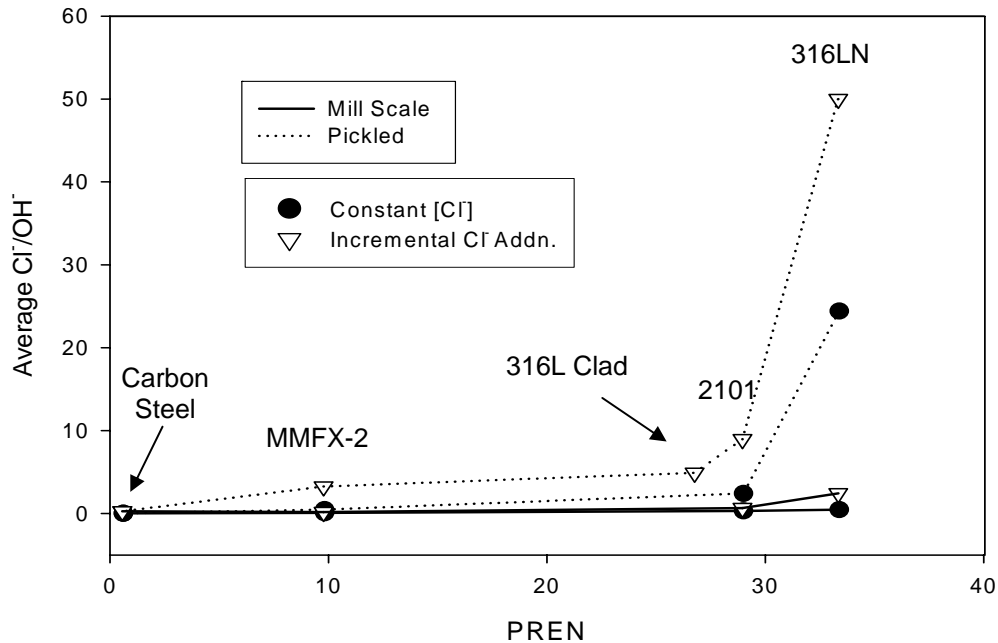

Figure 17. Chloride threshold results obtained from 316LN compared to carbon steel during incremental chloride addition and constant chloride potentiostatic testing. Experiments were performed at +200 mV vs. SCE in saturated Ca(OH)$_2$ with various amounts of NaCl added.

24

Figure 18. Summary of chloride threshold results from potentiostatic testing vs. PREN for candidate rebar types used in this study. Experiments were performed at +200 mV vs. SCE in saturated Ca(OH)$_2$ with various amounts of NaCl added.

Chloride Threshold after Artificial Aging

Enhanced passivity due to Ca(OH)$_2$ exposure before corrosion initiation was investigated by conducting chloride threshold tests on pre-aged samples. Samples were aged at +200 mV vs. SCE in saturated Ca(OH)$_2$ for 72 hours and tested using the constant chloride concentration testing method. This method allowed for precise control over the aging conditions as well as uniform duration of aging (prior to chloride introduction) and exposure to chlorides, for all samples tested. Age times greater than 2 days at +200 mV vs. SCE yield similar polarization resistance values to samples aged for 260 days (or greater) at OCP. Moreover, aging for greater than 2 days at +200 mV vs. was similar to long term OCP aging; greater than 260 days in this study and greater than 54 days (Abreu et al., 2006).   Hence, potentiostatic aging mimicked long term exposure as justified by polarization resistance. Results are reported in Figures 19 and 20. A grey data point was used for the highest value presented for the pre-aged 316LN stainless steel test (Figure 19), since the sample initially displayed a current value above the threshold, but later displayed persistent passivity. A low value of Cl$^-$/OH$^-$ = 20 was obtained from the shortest duration incremental chloride concentration test on 316LN, which is similar to that obtained from constant chloride testing (Cl$^-$/OH$^-$ = 24). However, the resistance to initiation for 316LN shows a large improvement with aging, with a conservative value of the chloride threshold of Cl$^-$/OH$^-$ = 100 obtained from pre-aged 316LN. The chloride threshold for carbon steel increased from Cl$^-$/OH$^-$ = 0.05 to Cl$^-$/OH$^-$ = 0.15 with pre-aging and MMFX-2 increased from Cl$^-$/OH$^-$ = 0.10 to Cl$^-$/OH$^-$ = 0.34 (Figure 20).   A greater improvement in the chloride threshold with aging was seen for higher alloyed bars (316LN and MMFX-2) than for carbon steel. For these bars, the chloride thresholds of pre-aged samples were very similar to those obtained from incremental chloride concentration chloride threshold testing (Figures 19 and 20).

25

Figure 19. Chloride threshold results of pre-aged 316LN (constant chloride test method) compared to un-aged samples (constant and incremental chloride testing methods). All pre-aging (3 days) and testing was conducted at +200 mV vs. SCE in saturated Ca(OH)₂.
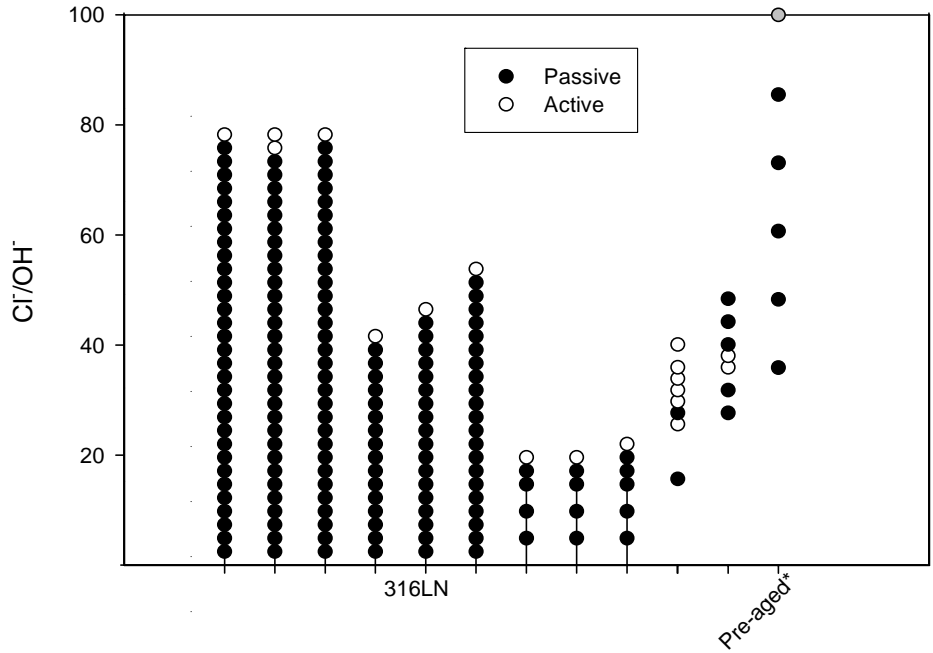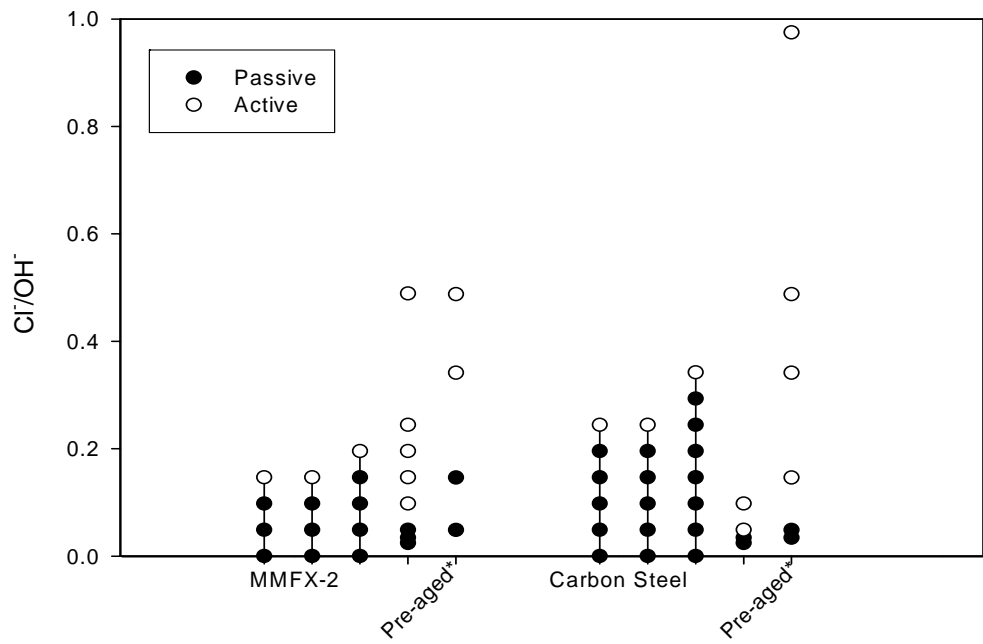

Figure 20. Chloride threshold results of pre-aged carbon steel and MMFX-2 (constant chloride test method) compared to un-aged samples (constant and incremental chloride testing methods). All pre-aging (3 days) and testing was conducted at +200 mV vs. SCE in saturated Ca(OH)₂.

Radial Propagation

Infinite Cathode: Potentiostat Control

Electrochemically induced radial corrosion propagation experiments were conducted on carbon steel, 316LN stainless steel, 2101, and MMFX-2. Two examples of the applied potential and resultant dissolution current data are shown in Figures 21-22. Following the first potential step to initiate and propagate corrosion across the entire anode area, the potential was incrementally stepped down to monitor the corrosion current at each potential. Carbon steel (shown in Figure 21) and MMFX-2 remained active following the first potential step until the OCP is reached and thus repassivation is not observed. For example, on carbon steel and MMFX-2 the OCP is reached at -0.55 (V) vs. SCE (~31,000 sec), after which the electrode becomes net cathodic for the remaining potential steps. In comparison, an example of an electrode that repassivates is seen in Figure 22 for 316LN, with repassivation starting at -0.15 V occurring at -0.2 (V) vs. SCE. Duplex stainless steel 2101 also remains active until -0.35 (V) vs. SCE (~ 24,000 sec), where the current drops by three orders of magnitude, indicating repassivation with subsequent passive dissolution at lower potentials. Repassivation is eventually followed by cathodic polarization upon further decreases in potential (below -0.4 (V) vs. SCE).

In order to obtain the rate of radial propagation via Faraday's law (*eqn. 5*) discussed above, it is first necessary to characterize the current (I) behavior at each potential step according to *eqn. 4*. It was seen that $I(E_{applied},t)$ only changed with potential and remained steady with time at each potential during active corrosion on all materials (examples of carbon steel and 316LN are shown in Figures 21-22) because pit geometry was approximately constant with time regardless of controlling factors. This was not seen during the first potential step to initiate pit growth where the current generally decayed with time. Here, the geometry changed with time suggesting a different controlling factor during early stages of pit growth. Compared to the initial potential step, the change in pit depth during subsequent potential steps was small. For the present analysis, only further pit growth following the establishment of a stable aggressive pitting environment is considered. Therefore, the dependence of $I(E_{applied})$ on t during active radial pit growth, following the first potential step, was determined to be $n = 0$, yielding:

$$I(E_{applied},t) = I^*(E_{applied})t^0 \qquad\qquad (eqn.\ 8)$$

The value of $I^*(E_{applied})$ at each potential step was determined for each material by calculating the average current value at a given potential (e.g., n = 0). Hence, the power law governing the radial growth of a single hemispherical pit based on *eqn. 5* was established with $n = 0$ as:

$$r = kt^{\frac{n+1}{3}} = kt^{\frac{1}{3}} \qquad\qquad (eqn.\ 9)$$

27
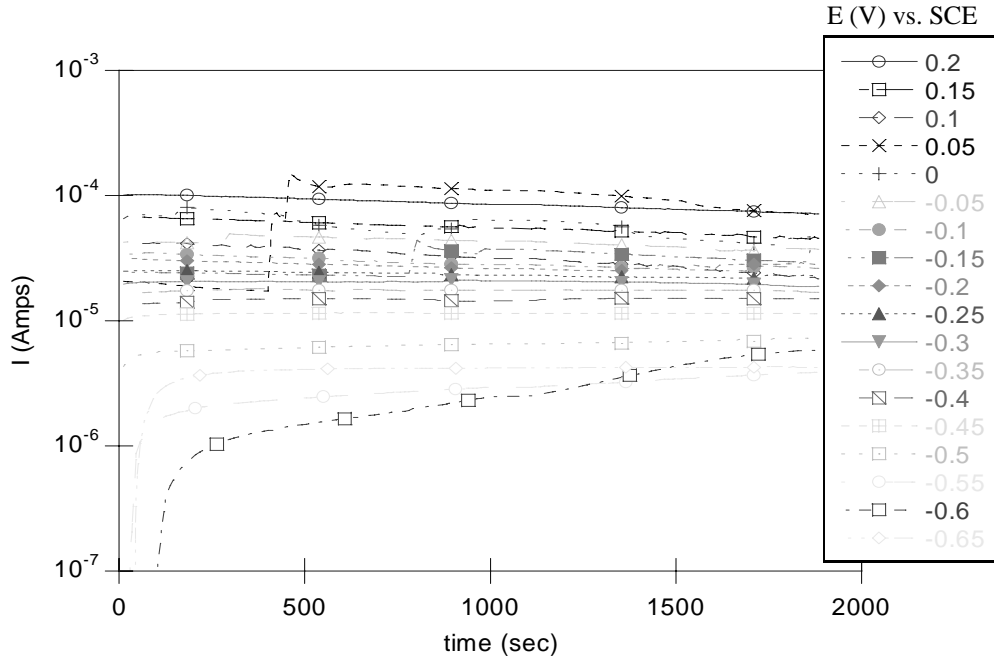
Figure 21. The resultant current at each applied potential on carbon steel, during an infinite cathode radial propagation experiment following the first step to initiate and propagate corrosion on the anode (exposed anode area ~0.5 mm^2). The current is approximately linear with time at each potential step. Some increase in the current is seen at low potentials (-0.6, -0.65 (V) vs. SCE) where the electrode became polarized cathodically.
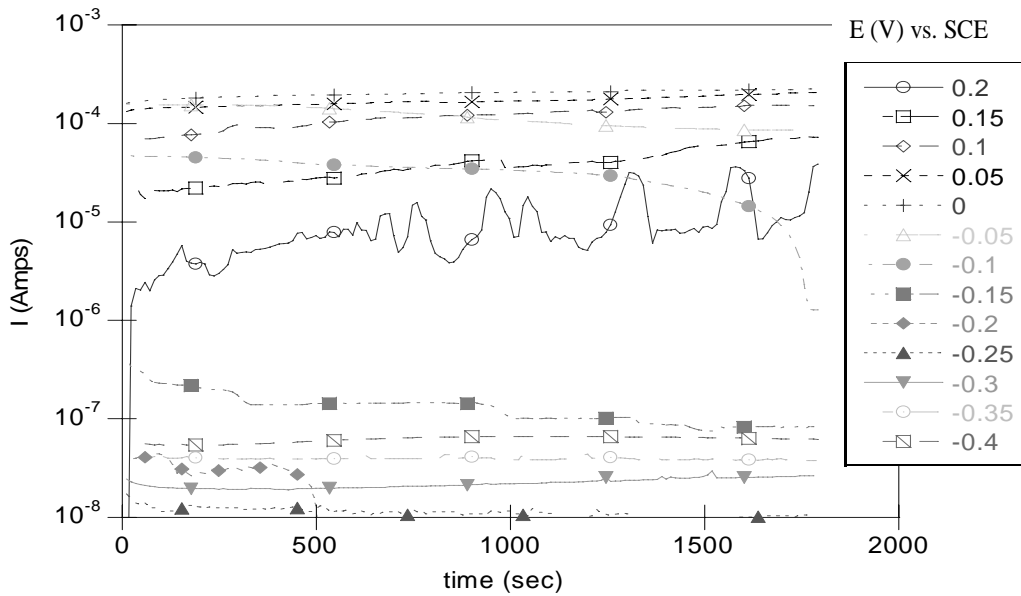
Figure 22. The resultant current at each applied potential on 316LN stainless steel, during an infinite cathode radial propagation experiment following the first step to initiate and propagate corrosion on the anode (exposed anode area ~0.5 mm^2). The current is approximately linear with time at each potential step. An abrupt decrease in current is seen at -0.1 (V) vs. SCE, when the electrode repassivates and subsequent potential steps exhibit significantly decreased current values.

28

Where k is now a potential dependent pit growth parameter given in *eqn. 5*, and t is time. $I^*(E_{applied})$ vs. $E_{applied}$ data following initiation is plotted for all materials in the potential range which displayed active pit growth (Figure 23). This was over a range of potentials that may be encountered in concrete during corrosion. All materials demonstrated linear I^* vs. $E_{applied}$ behavior, for the presented potential range. The linear dependency between $I^*(E_{applied})$ and $E_{applied}$ strongly suggests ohmic controlled pit growth in this potential range. Ohm's law can be used to calculate the effective governing ohmic resistance from the active pit, given by *eqn 10*, where R_{Ω} is the effective ohmic resistance in ohms:

$$E_{applied} = I^*(E_{applied}) \times R_{\Omega} \qquad (eqn.\ 10)$$

The value of R_{Ω} was calculated from the slope ($\Delta I^*/\Delta E_{applied}$), determined by a linear regression fit of I^* vs. $E_{applied}$ data from Figure 23, and is presented in Table 4.
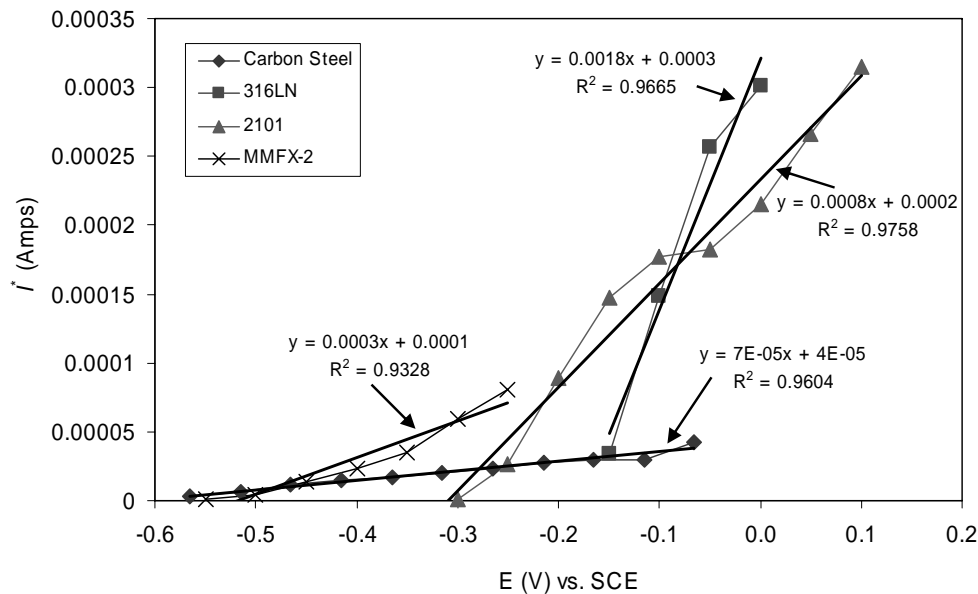
Figure 23. I^* vs. $E_{applied}$ **for all materials tested during incremental decreasing potential steps following the first potential step to induce corrosion damage (initial exposed area ~0.5 mm^2). The range of data presented is limited to that which active radial growth was observed. Linear I^* vs. $E_{applied}$ behavior was observed suggesting ohmically controlled pit growth. The experimental data was fitted using linear regression analysis to obtain the trendlines shown**.

Table 4. Summary of ohmic resistance (R_Ω) values, obtained from the slope of I^* vs. $E_{applied}$ data during stable pit growth.

Material	Test Environment	R_Ω (Ω)
Carbon Steel	Sat. $Ca(OH)_2$ + 0.1 M NaCl	14,285
MMFX-2	Sat. $Ca(OH)_2$ + 0.1 M NaCl	3,333
2101	Sat. $Ca(OH)_2$ + 1.0 M NaCl	1,250
316LN	Sat. $Ca(OH)_2$ + 2.0 M NaCl	556

Pit growth was assumed to evolve as a hemisphere with an increasing radius. This assumption was established based on previous work by other authors and verified during this study (Hunkler and Bohni, 1981; Newman and Franz, 1984; Wong and Alkire, 1990). The growth of hemispherical damage radius at one applied pit growth potential using *eqn. 9* is plotted in Figure 24 for each material tested assuming corrosion damage follows the power law of $r=kt^{1/3}$ (*eqn. 9*). Notice that the extent of radial growth was similar for all materials tested although the conditions for activation or corrosion were radically different. Generally, the incremental increase in radius of hemispherical damage volume became smaller with each decreasing potential step (not shown) for all materials. Additional radial growth effectively stops once repassivation occurs or the OCP is reached, and the increase in radius ≈ 0. The radius of hemispherical damage volume for carbon steel continued to increase at all potential steps tested until the OCP was reached, no further increase in radius was seen below -0.55 (V) vs. SCE. 2101 shows a greater increase in radius at each potential step compared to carbon steel at high potentials, but at -0.3 (V) vs. SCE repassivation occurs and there is a much smaller relative increase in radius. During subsequent potential steps, there was no further significant radial growth. MMFX-2 behaved very similarly to carbon steel at potentials below 0.1 (V) vs. SCE, while 316LN stainless steel displayed the highest resistance to pit growth and achieved repassivation at -0.2 (V) vs. SCE.

The pit growth parameter, *k,* was calculated from $I^*(E_{applied})$ vs. $E_{applied}$ data, using each materials specific equivalent weight and density, at each applied potential. In Figure 25, the parameter *k* for all materials tested is plotted versus the potential from which it was obtained. The obtained *k* values were potential dependent but similar for all materials (see Table 5). In addition, each material's threshold for repassivation from radial propagation is seen through a sharp drop in *k* value ($k \leq 4\times10^{-4}$ cm/sec$^{1/3}$) at a specified potential. This sharp drop signifies that radial growth has effectively stopped due to repassivation or that the electrode has gone cathodic. Radial penetration was effectively shut down on carbon steel and MMFX-2 at potentials below -0.55 (V) vs. SCE, 2101 was more resistant with radial growth turned off at -0.35 (V) vs. SCE, and 316LN was the most resistant displaying no significant growth below -0.2 (V) vs. SCE (Table 5).
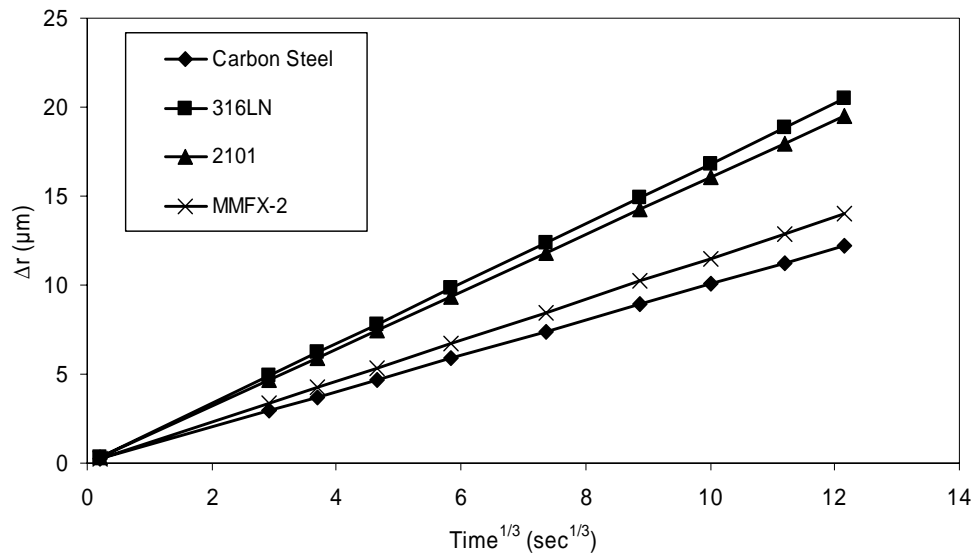
Figure 24. Calculated radial attack depth versus time$^{1/3}$ at 0.0 (V) vs. SCE, during radial corrosion propagation experiments following the first potential step to initiate corrosion damage. Attack depth is expressed as the radius of a growing hemispherical pit, for all materials tested.
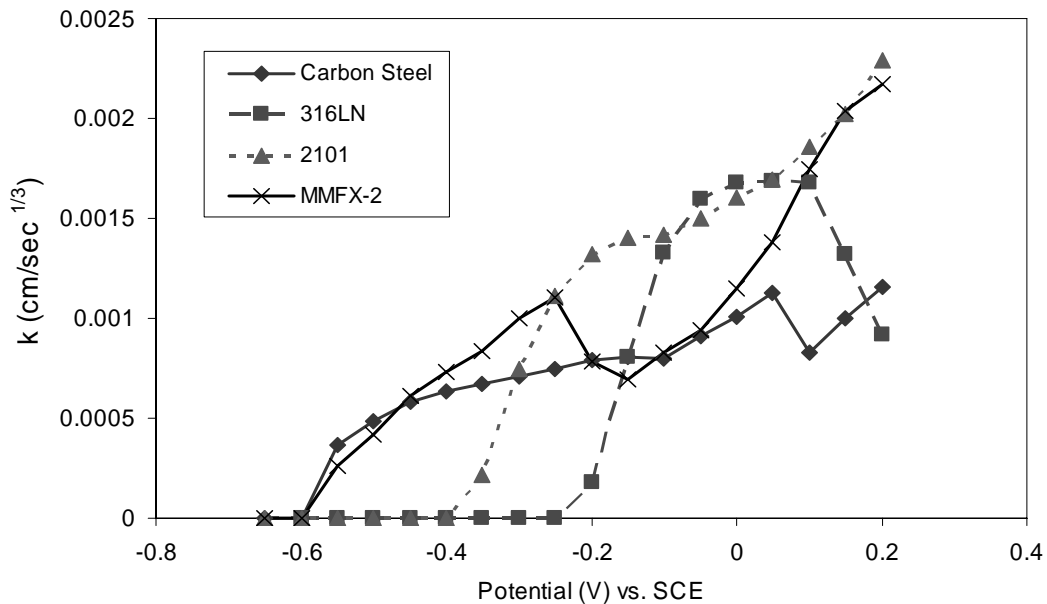
Figure 25. The calculated value of *k* is plotted vs. the potential at which it was determined assuming power law (*r=kt$^{1/3}$*) pit growth behavior from electrochemical radial propagation tests conducted on carbon steel, MMFX-2, 2101, and 316LN rebar.

Table 5. The constant *k*, from the radial growth power law $r = kt^n$, calculated from experimentally determined I^* values at each prescribed $E_{applied}$.

| $E_{applied}$	k (cm/sec$^{1/3}$)			
(V) vs. SCE	Carbon Steel	316LN	2101	MMFX-2
0.2	1.15E-03	9.21E-04	2.29E-03	2.17E-03
0.15	9.98E-04	1.32E-03	2.02E-03	2.04E-03
0.1	8.32E-04	1.68E-03	1.85E-03	1.75E-03
0.05	1.13E-03	1.69E-03	1.70E-03	1.38E-03
0	1.01E-03	1.68E-03	1.60E-03	1.15E-03
-0.05	9.07E-04	1.60E-03	1.50E-03	9.44E-04
-0.1	8.01E-04	1.33E-03	1.41E-03	8.29E-04
-0.15	8.02E-04	8.09E-04	1.40E-03	6.94E-04
-0.2	7.89E-04	*repassivation*	1.32E-03	7.83E-04
-0.25	7.46E-04		1.11E-03	1.11E-03
-0.3	7.09E-04		7.45E-04	9.98E-04
-0.35	6.75E-04		*repassivation*	8.39E-04
-0.4	6.38E-04			7.31E-04
-0.45	5.85E-04			6.11E-04
-0.5	4.82E-04			4.21E-04
-0.55	*OCP*			*OCP*

Lateral Propagation

Mapping the Spread of Active Corrosion

Testing was performed to examine lateral spreading of corrosion on carbon steel, 316L stainless steel, and simulated defective stainless steel clad rebar by utilizing 5x20, 100-wire, coupled electrode arrays. Testing was conducted under two electrochemical conditions "natural" (all electrodes 0.2 (V) vs. SCE) and "activated columns" (selected columns at 0.5 (V) vs. SCE), as defined above.

An example of results from experiments conducted on carbon steel with all electrodes held at +200 mV vs. SCE in both saturated $Ca(OH)_2$ + 0.2 M NaCl and saturated $Ca(OH)_2$ + 0.2 M NaCl with sand/glass beads added is discussed below. The response of carbon steel is similar under both environmental conditions: corrosion initiates quickly (< 100 sec) and spreads at a similar rate across the entire electrode until all electrodes undergo active corrosion. The fact that corrosion spreads easily in both environments suggests that there is little effect on mass transport due to the presence of sand + glass beads in the electrolyte. It could be hypothesized that little effect would be seen in concrete. A similar experiment was conducted under the activated column condition, where electrode columns 8 and 9 (of 20) were held at 0.5 V vs. SCE (all others at 0.2 V). Corrosion initiates and spreads at similar rates, but not necessarily from electrode columns held an elevated potential. For the experiment conducted in solution only, corrosion spreads laterally from the activated columns. During the experiment conducted in sand

+ glass beads corrosion initiated quickly on the activated columns but also towards each edge of the electrode array. Corrosion then spread quickly until the entire MEA was depassivated.

Similar lateral corrosion experiments were also conducted on 316L stainless steel and the simulated defective stainless steel clad array (simulating defects in the clad layer that expose the carbon steel core). The experimental environment used for the stainless steel array was considerably more aggressive than what was used for carbon steel and defective clad arrays since no corrosion was initiated on the stainless steel electrodes in testing conducted in saturated $Ca(OH)_2$ (pH 12.6), regardless of chloride concentration. Therefore, the electrolyte used for stainless steel was changed to 3 M NaCl (pH 7). Despite the much more aggressive environment, stable active corrosion was only observed on 316L electrodes held at 1 V vs. SCE, with virtually no corrosion activation on adjacent electrodes, that were held at 0.2 V vs. SCE. Electrodes that maintained depassivation showed localized attack; all others were largely unaffected. These results suggest that corrosion will spread across carbon steel rebar but not stainless steel rebar even with defect sites that expose carbon steel, in the case of clad bar. The stainless steel electrodes in the simulated defective clad rebar MEA showed similar results to the MEA constructed entirely of 316L stainless steel. The carbon steel electrodes simulating the clad defect initiated quickly, but the local environment established during active corrosion was not aggressive enough to cause active corrosion on any of the nearby stainless steel electrodes. The carbon steel electrodes displayed general corrosion over the entire electrode, and no attack was seen on the passive stainless steel electrodes.

In summary, carbon steel depassivated readily and corroded over broad areas while corrosion of stainless steel only occurred under extremely aggressive conditions (environmentally and electrochemically) and was confined localized attack, which did not spread to adjacent electrodes. In simulated defective stainless steel clad array experiments no effect of corrosion initiation was observed on stainless steel electrodes due to the influence of stable corrosion on neighboring carbon steel electrodes.

Pitting Factor

The pitting factor was calculated for each rebar alloy following corrosion exposures under electrochemical acceleration. Figure 26 shows that pitting occurs on 316LN while almost uniform general corrosion occurs on carbon steel. Therefore, 316LN experienced the highest pitting factor accompanied with the formation of high aspect ratio pits with minimal corrosion of passive surfaces away from pits (Figure 27). In contrast, carbon steel had the lowest pitting factor (corrosion was more uniform and widespread) and the damage morphology approached general corrosion when compared to the other alloys tested. 2101 and MMFX-2 duplex steels displayed similar behavior in both potential response during galvanostatic induced corrosion and the respective pitting factor values. After increasing exposure time, the pitting factor was observed to decrease with time on all materials, indicative of some spread in corrosion or pit coalescence as a larger fraction of the surface area is attacked by propagating corrosion.

| Carbon Steel | MMFX-2 | 2101 Stainless Steel | 316LN Stainless Steel |
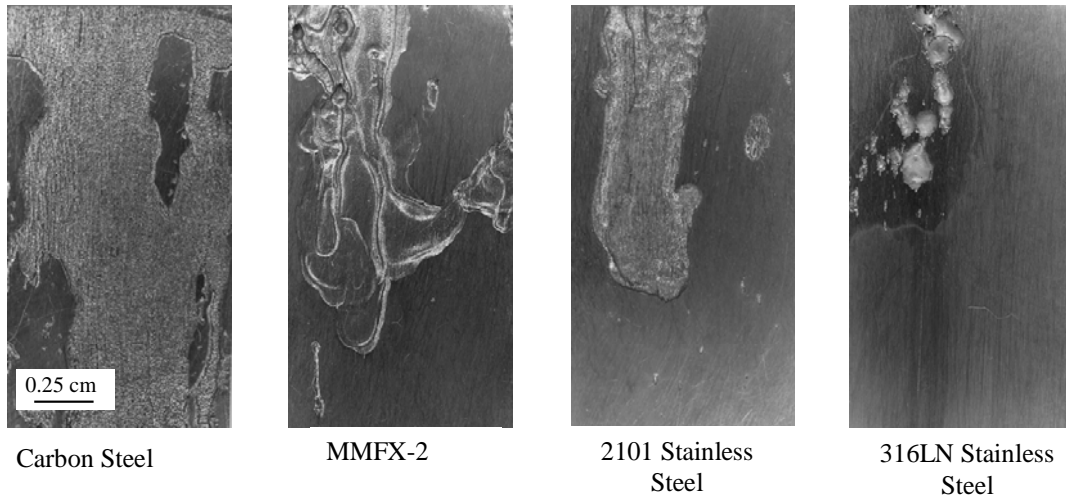
Figure 26. Macro photographs of pitting factor test samples galvanostatic induced corrosion propagation. Identical sized samples were held at 0.0012 Amps/cm^2 for 24 hours and cleaned to remove corrosion products.
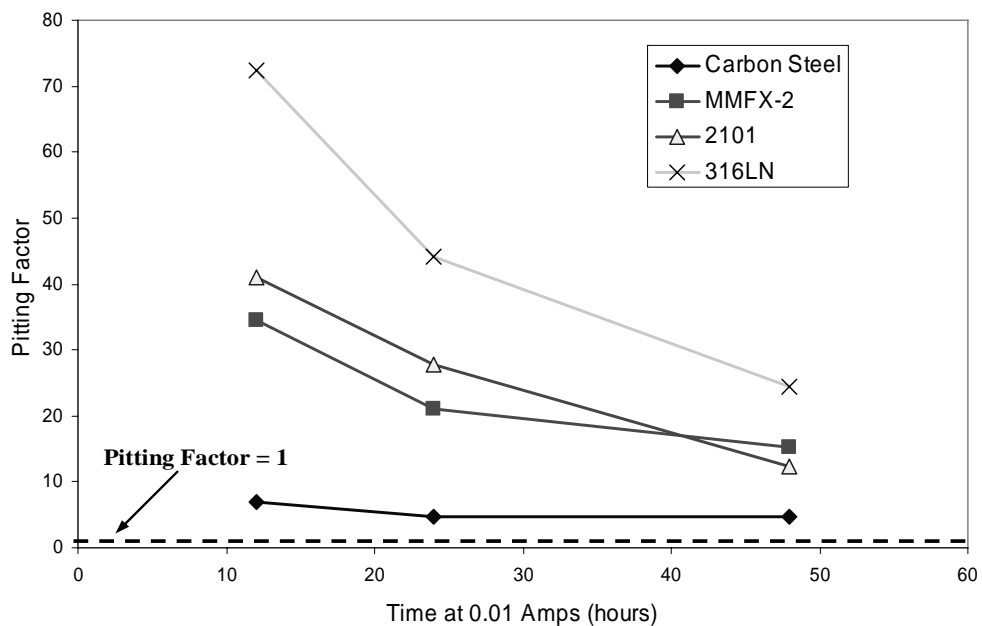
Figure 27. Pitting factors obtained for all rebar materials tested. Experiments were conducted at 0.0012 Amps/cm^2 for 12, 24, and 48 hours. A pitting factor of 1 signifies general corrosion with 100% of the area active. Larger numbers indicate increasingly localized corrosion attack.

Corrosion Product Characterization

An important consideration regarding corrosion resistant rebar is the structure and type of corrosion products that may form once active corrosion occurs. Based on the alloy compositions of the materials considered, a preliminary survey of the relevant properties of possible oxides which may be formed was conducted (Table 6). Table 6 indicates that oxide forms of the most

34

abundant alloying elements found in MMFX-2, 2101, and 316LN stainless steel (Cr, Mn, Ni, and Mo) posses similar densities to the oxides of carbon steel (Fe). Additionally, the specific volume per 10 g of the alloying element oxides is typically less than those of Fe, with the exception of CrO_3 (Figure 28). This result demonstrates that corrosion products formed during the corrosion propagation phase would have a roughly equivalent specific volume regardless of the type and amount of different oxides produced. Oxides that develop during active corrosion were examined. XRD scans were performed on corrosion products collected from carbon steel, MMFX-2, 2101, and 316LN stainless steel rebar samples (Figure 29). Four relatively strong, narrow peaks are seen in the scan performed on the corrosion products of 316LN only. These peaks were identified as NaCl and are likely present from residual testing solution on the corrosion products, which evaporated during drying leaving behind some NaCl crystals. The NaCl peaks present in the 316LN scan are not present in the other corrosion products tested likely because the solution used during corrosion product production had a much higher chloride content than the solution used for other materials, based on the chloride threshold. With the exception of the NaCl peaks, XRD scans on corrosion products from all materials examined were virtually identical. The relatively weak broad peaks indicate that the corrosion products formed are not completely crystalline and are similar, regardless of the rebar material they came from.

Table 6. Density of potential corrosion products (Lide, 2005).

Oxide/Hydroxide	Density (g/cm^3)	Oxide/Hydroxide	Density (g/cm^3)
Fe	7.87	Mn	7.3
FeO (II)	6	MnO (II)	5.37
Fe_2O_3 (III)	5.25	MnO_2 (IV)	5.08
Fe_3O_4 (II, III)	5.17	Mn_2O_3 (III)	5
FeO(OH) (III)	4.26	Mn_3O_4 (II, III)	4.84
$Fe(OH)_2$ (II)	3.4	MnO(OH) (III)	4.3
$Fe(OH)_3$ (III)	3.12	$Mn(OH)_2$ (II)	3.26
Cr	7.15	Ni	8.9
Cr_2O_3 (III)	6.1	NiO (II)	6.72
Cr_3O_4 (II, III)	6.1	$Ni(OH)_2$ (II)	4.1
Cr_2O_3 (III)	5.22	Mo	10.2
CrO_2 (IV)	4.89	MoO_2 (IV)	6.47
CrO_3 (VI)	2.7	MoO_3 (VI)	4.7
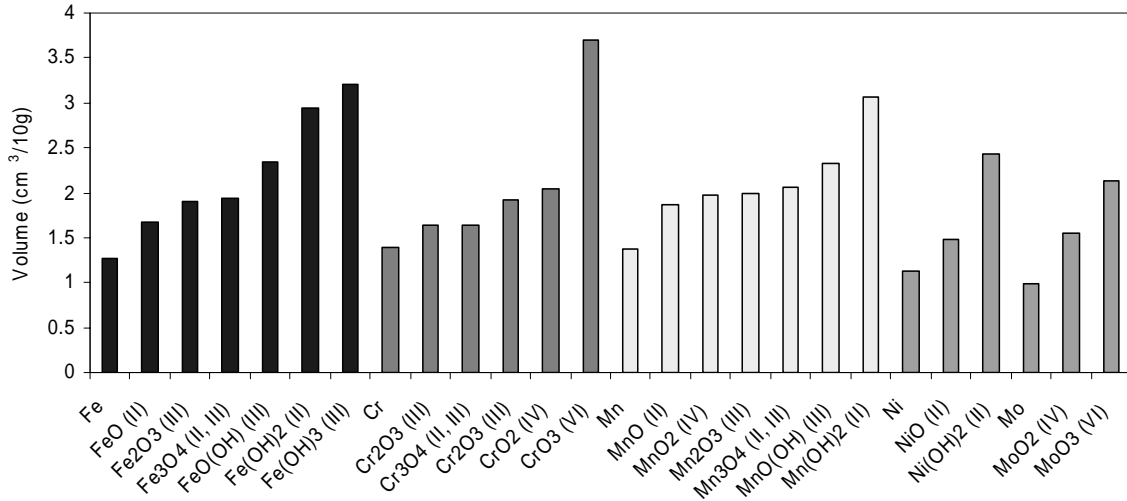
Figure 28. Specific volume of oxides and hydroxides potentially formed during active corrosion, based on the rebar compositions considered for this study.
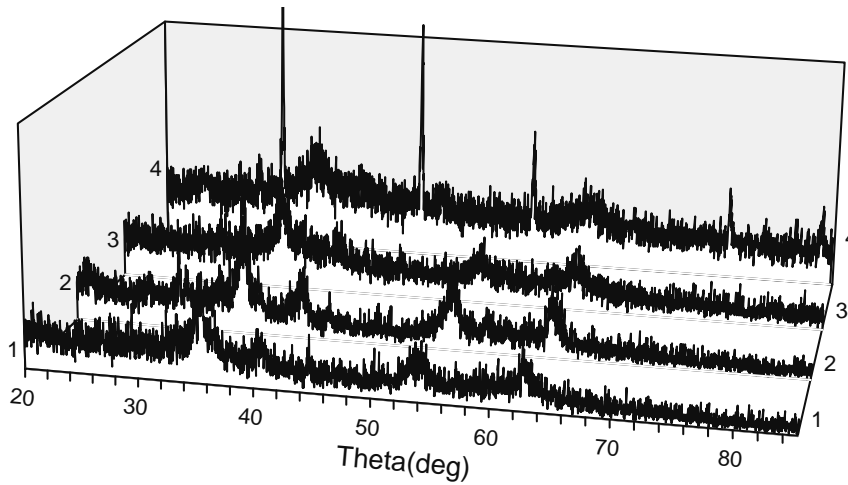
Figure 29. XRD scans conducted on the corrosion products generated from carbon steel (1), MMFX-2 (2), 2101 (3), and 316LN stainless steel rebar (4).

DISCUSSION

Effect of Material Composition on Chloride Threshold

The potentiostatic test methods performed during this study provided conservative results but produced differences in the chloride thresholds that depended not only on material composition but also on surface condition and the presence of any microstructural or physical

defect. In the case of stainless steel clad rebar, the "physical" weakest link present in the system determined the chloride threshold despite the high PREN number of 316L cladding (e.g., PREN = 26.8). For instance, the chloride threshold obtained from potentiostatic tests did not correlate linearly with the PREN of all the materials tested (Figure 18). Prior results regarding the crevice corrosion and pitting resistance of a variety of stainless steels, including some duplex stainless steels such as 2205, show a linear correlation between PREN and critical pitting temperature (CPT) as well as critical crevice temperature (CCT) (Sedriks, 1996). The composition of each phase in the duplex microstructure of many modern duplex stainless steels is balanced such that resistance is linearly proportional to a PREN calculated based on overall composition. This would suggest that pickled 2101 (PREN = 29) should have a chloride threshold similar to that obtained for 316LN (PREN = 33.3). However, the results obtained from incremental chloride testing showed the chloride threshold for pickled 2101 was approximately half that of 316LN (Figure 12). One possible explanation for this discrepancy is the accidental formation of detrimental phases, including sigma phase, in the duplex microstructure due to inadvertent slow cooling through the temperature range of 700-900°C. The other possibility is that PREN number does not scale linearly with local corrosion resistance in simulated concrete even though it does in other chloride containing environments. It is worth noting that a separate heat of pickled 2201 duplex stainless steel tested independently in another study also does not perform nearly as well as AISI 316 either (Lysogorski et al., 2005). Metallographic characterization on the 2101 used in this study has not substantiated the possibility of sigma phase, although some uncertainty exists since the exact heat treatment history of this batch of the alloy is not known.

Effect of Surface Condition on Chloride Threshold

The presence of mill scale on the rebar surface had a profound detrimental effect on the chloride threshold of alloyed rebar materials compared to a pickled surface. For all rebars tested, the presence of mill scale resulted in a chloride threshold similar to that of carbon steel. The benefit of pickling increases with PREN as shown in Figures 16-18. In order to reveal this effect, it is clear that that the surface condition of the rebar must be considered, as opposed to simply testing the polished surface of the base material. The explanation for the mill-scale effect is complex. The high temperature oxide that develops is less adherent and produces a chromium depleted surface layer (Stott and Wei, 1989). The protective effects of the passive film associated with a thin compact chromium oxide layer are greatly diminished with presence of a mill scale on the surface. Corrosion that is initiated more easily on the Cr-depleted mill scale surface may lead to formation of an aggressive environment and subsequent activation of the base material under conditions where it would not normally occur. Therefore, pickling must be strongly considered for alloyed rebar materials in order to passivate the surface and increase the corrosion resistance.

Influence of Aging on Chloride Threshold

Comparison of polarization resistance (R_p) results obtained from this study with those published by other authors has verified that the aging regiment used for this study simulates long term aging, greater than 260 days at OCP in solution and similarly 2 years in concrete (Gu et al., 1996). Samples passivated under anodic polarization for short times displayed similar R_p values to those aged at OCP for long times and hence the degree of passivity obtained during aging for this study is comparable to long term aging at OCP. Aging did improve chloride threshold

values for 316LN (Figure 19) and a slight improvement was observed on carbon steel and MMFX-2 (Figure 20). Therefore, the chloride thresholds obtained likely represent conservative values when compared to rebar embedded in concrete for many more years prior to corrosion initiation.

Influence of Defects in Cladding on Chloride Threshold

Stainless steel clad rebar is attractive in theory because when the cladding layer is intact it should behave identically to solid stainless steel rebar. Results from chloride threshold testing did not confirm the similarity of intact clad and solid stainless steel, but instead demonstrated that corrosion initiation is dictated by the "weakest link" present (Figure 13). The trend in chloride thresholds was as follows: U-with a drilled hole exposing the carbon steel ($Cl^-/OH^- = 0.25$) < straight bar with the cut end exposed ($Cl^-/OH^- = 0.73$) < Intact U-bend ($Cl^-/OH^- = 4.9$) < solid 316LN stainless steel ($Cl^-/OH^- = 20$). The intact clad U-bend chloride threshold was surprising low, possible due to metallurgical defects and crevices (> 1mm width at opening) present at the seam of the stainless steel cladding (Figure 14). These weak spots likely develop during fabrication of the stainless steel sleeve in which carbon steel granules are packed. It is possible that improvements in clad rebar fabrication technique will eliminate the premature initiation on the clad layer seen in this study. However, additional chloride threshold testing would be necessary to verify such a claim.

The initiation and propagation behavior of clad bar must be considered to evaluate their overall effectiveness. Although the threshold for corrosion initiation was lower than expected for intact bar, additional benefits of cladding may be realized during the propagation stage. Defects in the cladding (either mechanically or corrosion induced) must propagate to a critical extent to damage the surrounding concrete. The issue of whether or not corrosion initiated at defects will spread across the clad layer, increasing the amount of corrosion products generated, is addressed more fully in the propagation section.

Impact of Chloride Threshold and Modeling the Predicted Time to Initiation

Given the difference in chloride thresholds between plain carbon steel and alloyed rebar materials; it is of interest to consider the relative extension of the time until initiation of corrosion when rebar with a higher corrosion resistance than carbon steel is implemented. For an increase in chloride threshold (expressed as Cl^-/OH^- molar ratio) from 0.8 for plain carbon steel to 20 for solid stainless steel, how long does it take for the Cl^-/OH^- molar ratio in the concrete pore solution adjacent to an embedded rebar to reach the chloride thresholds described? Further, how much longer is the time until initiation if a corrosion resistant rebar material is used? Various models based on Fick's second law of diffusion have been used to predict chloride ingress in concrete (Bertolini et al., 2004). Such a calculation was performed based on a finite difference solution to Fick's second law. The code was provided by the Computer Integrated Knowledge System (CIKS) developed by Bentz et al. (Bentz et al., 1996). Modeling results have correlated well with experimental data obtained from chloride analysis of core samples in short term experiments however, experimental confirmation for long time periods (greater than 100 years) is not available.

The initiation time was calculated for the case of carbon steel compared to corrosion resistant steel. No chloride binding was assumed and the coefficient of diffusion was constant over time, taken to be $1*10^{-12}$ m^2/sec. The thickness of the concrete structure was set at 0.5 m and rebar was considered to be 50 mm deep, according to the ACI guide for durable concrete exposed to de-icing salts (ACI, 1994). The surface chloride content was input as a time varying square wave function with a Cl$^-$/OH$^-$ ratio of 100 ($C_{0,1}$ = 3.5 Mol.) for X days (t_1), followed by a Cl$^-$/OH$^-$ ratio of 0.29 ($C_{0,2}$ = 0.01 Mol.) for 365-X days (t_2), Figure 30a. This condition simulated periodic seasonal application of de-icing salts followed by low chloride exposure during the remainder of the year. Aggressive values for non-coastal concrete exposed to de-icing salt were chosen for the coefficient of diffusion and the surface concentration function to maintain a conservative approach to estimating the time until corrosion initiation. Additionally, the chloride threshold used for stainless steel was a lower bound (Cl$^-$/OH$^-$ ratio of 20) obtained from testing during this study and the chloride threshold for carbon steel (taken as a Cl$^-$/OH$^-$ ratio of 0.8) was an upper bound of results from simulated pore solution testing obtained from previously published results (Hausmann, 1967; Gouda and Halaka, 1970; Goni and Andrade, 1990; Alonso et al., 2000; Li and Sagüés, 2001). Under these conditions with a t_1 value of 120 days, 8 years was the time required to reach the chloride threshold of carbon steel at a depth of 50 mm. Approximately 103 years would be required to reach a Cl$^-$/OH$^-$ ratio of 20 at a depth of 50 mm- a conservative value for the chloride threshold of 316LN stainless steel. Figure 30b shows the effect of t_1 on the time to initiation. It can be seen that the time to initiation for stainless steel increases rapidly to values much greater than 100 years as t_1 drops below 120 days, which corresponds to nearly 4 months at constant high surface chloride concentration. Although this model assumes uniform intrinsic concrete properties and ignores chloride egress phenomena over the time period of consideration, it is an encouraging prediction when considering the 75-100 year lifetime design goal for new concrete structures.

The time to initiation was calculated for hypothetical corrosion resistant materials with Cl$^-$/OH$^-$ threshold concentrations of 0.1, 1, 10, and 20 at a t_1 step size of 120 days. The times to initiation for the chloride thresholds considered are shown in Table 7. An increase in hypothetical chloride threshold from 0.1 to 1 provides only a minor extension of time to initiation (4.3 years). However, substantial gain in time until initiation is obtained for a material that increases the chloride threshold over the range from 1 to 20. Moreover, in order to reach a design goal of 100 years before initiation the reinforcement should have a chloride threshold of at least Cl$^-$/OH$^-$ = 20.

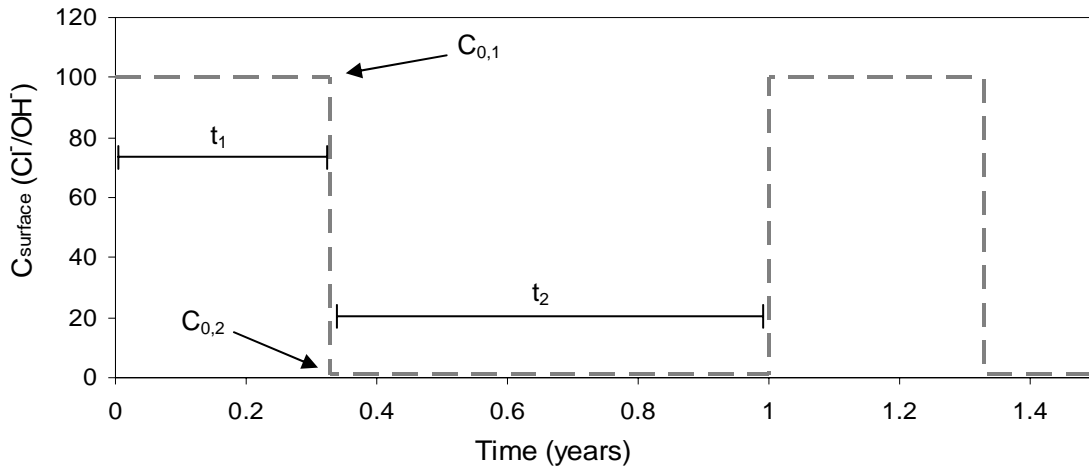**Figure 30(a). An example of the surface chloride concentration inputs used to model the time to corrosion initiation. The surface concentration is a square wave repeated yearly.**
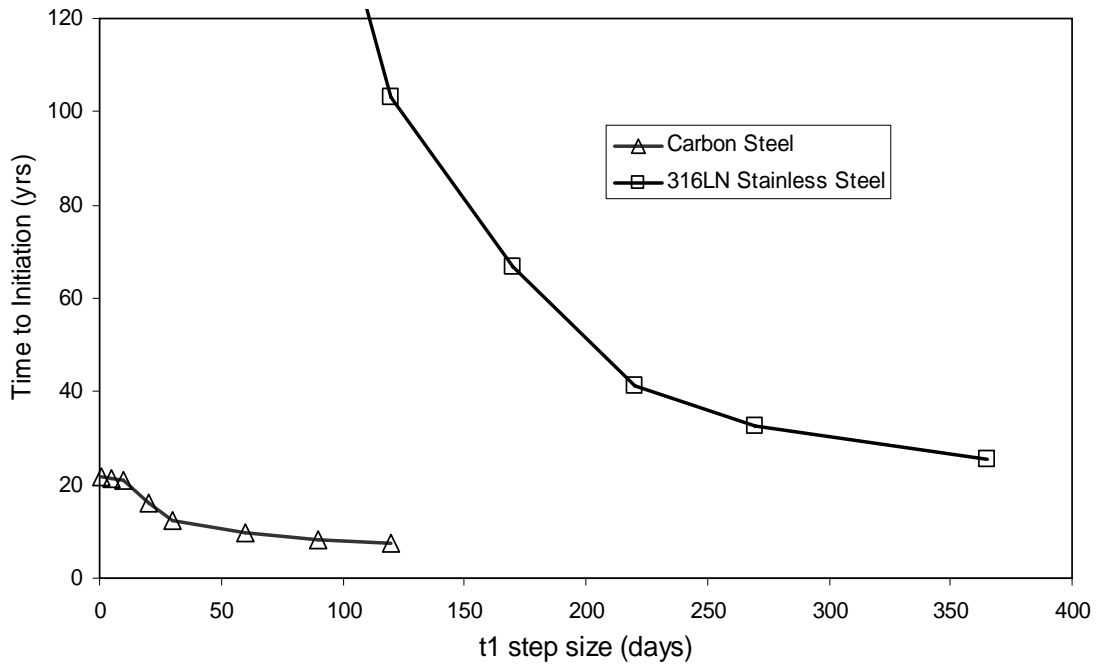

Figure 30(b). Influence of t1 duration on the time to initiation for stainless steel and carbon steel. The chloride threshold for carbon steel was assumed as $Cl^-/OH^- = 0.8$ and $Cl^-/OH^- = 20$ for stainless steel.

40

Table 7. Hypothetical chloride induced corrosion initiation times for various materials with a salting period of 120 days

Material Chloride Threshold (Cl⁻/OH⁻)	Time until initiation (years)
0.1	3.9
1	8.2
10	37.1
20	100

## Radial Corrosion Propagation in Concrete Compared to Ca(OH)$_2$ Solution

Pit growth was ohmically controlled for all materials and the factor dominating the controlling ohmic resistance was the resistance of the bulk solution. The linear relationships determined from fitting the experimental $E_{applied}$ *vs.* I^* values (Figure 25) were used to model $E_{applied}$ *vs.* I^* behavior for each material considered. Furthermore, model determined I^* values, together with the relevant material properties ($E.W., \rho$) were used to calculate k values (according to *eqn. 6*) as a function of $E_{applied}$ that would be applicable (Figure 25). The factor k is dependent on $E.W., \rho$, and I^* *(at $E_{applied}$)* where $I^* = E_{applied}/R_\Omega$. The material dependent terms *E.W. and ρ used* in the k relationship were very similar for all materials considered (Table 8). Elements less than 1 wt% of the overall composition were neglected in calculation of the *E.W.* and a valance of 2 was assumed for Fe (Fe^{2+}), Ni (Ni^{2+}), and Mn (Mn^{2+}); and 3 for Cr (Cr^{3+}) and Mo (Mo^{3+}). The k values determined from this model effectively predict the experimentally obtained k data (Figure 31). However, they are valid only for potentials that a material is susceptible to radial corrosion, i.e., above the shut-off potential as given in Table 9, depending on the corrosion resistance of the material.

Table 8. Density and equivalent weight for all materials considered for radial corrosion propagation experiments.

Material	ρ (g/cm³)	E.W. (g/equiv.)
Carbon Steel	7.8	28.21
316LN	8.0	25.68
2101	7.8	25.11
MMFX-2	7.9	26.68

Table 9. Material specific radial corrosion growth shut-off potentials, below which the radial corrosion model is not valid.

Material	Shut-off Potential (V) vs. SCE
Carbon Steel	-0.55
316LN	-0.2
2101	-0.35
MMFX-2	-0.55
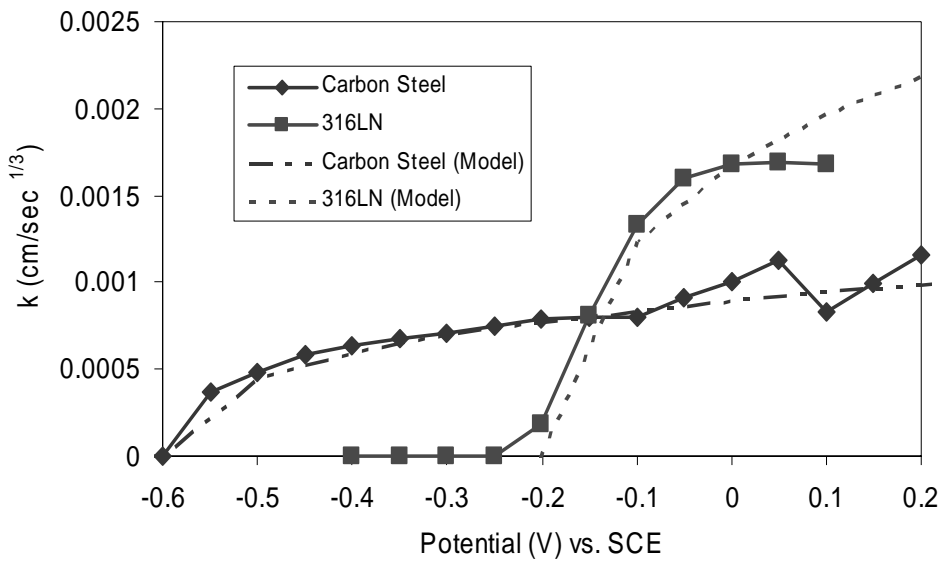
Figure 31. Assuming power law pit growth behavior ($r=kt^{1/3}$), the calculated model value of k is compared to the experimentally determined value of k as a function of potential (Figure 25), plotted for carbon steel and 316LN stainless steel. Corrosion attack geometry was assumed to be a hemisphere in all cases.

Since it has been shown that radial corrosion propagation is ohmically controlled and the origins of the ohmic resistance have been determined, it is now possible quantitatively anticipate the radial growth behavior in actual concrete media instead of $Ca(OH)_2$ solution. Prediction of the radial propagation behavior in concrete media was accomplished by converting I^* values obtained in $Ca(OH)_2$ solution over the same potential range to the applicable values in concrete by accounting for the increased resistance of concrete compared to the $Ca(OH)_2$ solution. The repassivation potential is assumed to be similar in both $Ca(OH)_2$ and concrete.

In order to translate the results to concrete, the R_Ω obtained from testing in Ca(OH)$_2$ (*eqn. 10,* Table 4) was substituted with an appropriate R_Ω for concrete with a similar chloride concentration, to obtain a new I^* (via *eqn. 10*) which accounted for the theoretical added resistivity in the bulk environment. To accomplish this conversion, R_Ω from Ca(OH)$_2$ (Table 4) was divided by the solution resistivity to obtain a resistance shape factor (Table 10). This shape factor was then multiplied by the resistivity of concrete plus a similar chloride concentration as used in solution testing obtained from data reported by Hunkler (Hunkler, 1996), to obtain a new R_Ω for concrete. R_Ω for concrete was then used to obtain a new I^* (in concrete) using Ohm's at each $E_{applied}$. This new I^* in concrete was then used to recalculate k (via. *eqn. 6*) to predict radial propagation corrosion behavior for each material in a concrete environment (Figure 32). The resistivity value differs for each material in concrete because the threshold chloride level differs.

Table 10. Summary of test environment solution resistivity and shape factor during radial corrosion propagation testing and the expected concrete resistivity with similar concentrations of free chloride.

Material	Test Environment	φ_{soln} (Ω-cm)	λ (cm^{-1})	$\varphi_{concrete}$ (Ω-cm)
Carbon Steel	Sat. Ca(OH)$_2$ + 0.1 M NaCl	48	306.1	2400
316LN	Sat. Ca(OH)$_2$ + 2 M NaCl	6	110.9	600
2101	Sat. Ca(OH)$_2$ + 1 M NaCl	12	136.8	1200
MMFX-2	Sat. Ca(OH)$_2$ + 0.1 M NaCl	48	102.9	2400

It should be noted that the effect of chloride content on concrete resistivity is secondary compared to the effect of moisture content (Hunkler, 1996; Polder and Peelen, 2002). Moreover, the values used for concrete resistivity were in the lower range of values typical for concrete with varying degrees of moisture content (Hunkler, 1996; Bentur et al., 1997; Polder and Peelen, 2002). Although the resistivity of concrete decreases with increasing moisture content, the diffusion coefficient of O$_2$ decreases as well. Any effects of decreased O$_2$ diffusion to cathodic sites on the coupled anodic dissolution rate were not considered in this analysis. Moreover, I^* (and thus k) varied with $E_{applied}$ in a somewhat material dependent linear fashion despite ohmically controlled pit growth, which is somewhat unusual for an ohmic controlled process. The material dependency of k was inversely related to the chloride threshold and hence k is dependent on the resistivity of the concrete environment, which itself is influenced by the chloride content required to cause corrosion initiation. For instance, carbon steel had the lowest resistance to corrosion initiation, highest resistivity (test environment was saturated Ca(OH)$_2$ + 0.1M NaCl) and thus the highest resistance to radial penetration (e.g., lowest k for a given $E_{applied}$). Conversely, 316LN had the highest chloride threshold, lowest bulk environment resistivity, and lowest resistance to pit growth (e.g., highest k for a given $E_{applied}$). Hence, the constant k is strongly influenced by the ionic transport properties of the concrete environment. A change in the ionic transport properties between the cathode and active corrosion site anode would control effect an ohmically controlled current ($I^*(E_{applied})$) value through its direct influence on R_Ω, as seen in Figure 32. Thus, a model has been formulated that describes rate of

radial corrosion penetration with time (cm/sec), based on the physical properties and electrochemical behavior of each rebar alloy considered. This model is only applicable once stable corrosion has been established and in the relevant potential range which a specific alloy is susceptible to sustained active corrosion.

The data analysis in this section regarding ohmically controlled pit growth behavior specific to each material can be used to rank each material in terms of their relative radial corrosion propagation behavior. Two metrics are presented to describe a materials response to active pit growth: resistance to radial corrosion propagation expressed by a potential threshold and rate of penetration during radial corrosion. The resistance to radial corrosion propagation is characterized by the relative radial attack shut off potential. The shut off potential was determined to be the potential below which an electrode was repassivated or became cathodically polarized during propagation experiments (Table 9). The ranking of the materials tested according the resistance to radial corrosion propagation metric is as follows (high to low):

316LN stainless steel > 2101 duplex stainless steel > MMFX-2 = Carbon steel

According to the second metric, rate of penetration during radial corrosion, a high k value indicates faster rate of penetration and thus a lower (worse) ranking. The ranking of materials for a specific $E_{applied}$ (e.g., +0.0 (V) vs. SCE) is as follows (best to worst):

Carbon steel > MMFX-2 > 2101 duplex stainless steel > 316LN stainless steel

Regarding the second ranking metric, it should be noted that a material may be considered only if the chosen $E_{applied}$ is above that materials radial attack shut off potential, shown in Table 9.
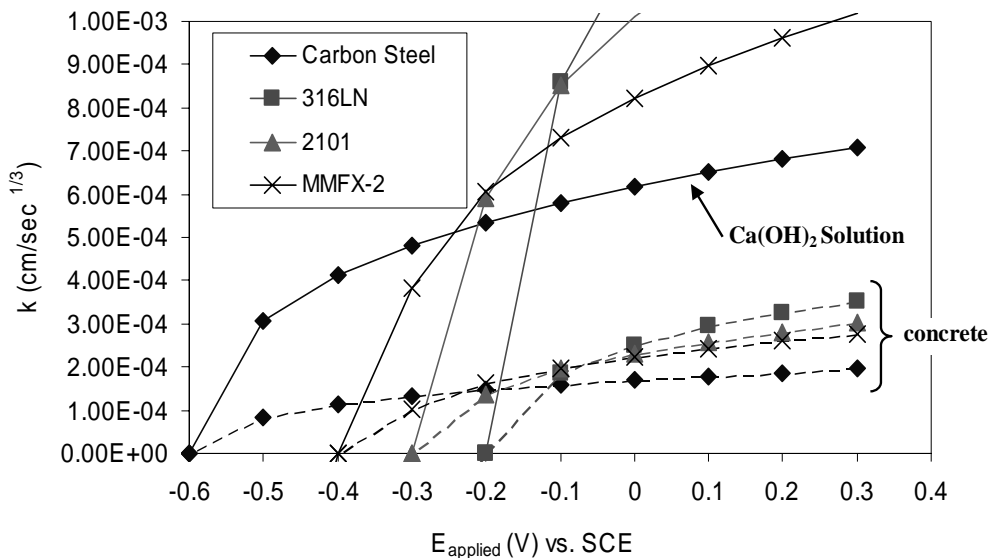

Figure 32. The theoretical k behavior in concrete (with greater resistivity compared to saturated Ca(OH)$_2$ solution) is plotted as a function of potential for all materials tested, assuming power law ($r=kt^{1/3}$) pit growth behavior. Corrosion attack geometry was assumed to be a hemisphere in all cases.

44

Lateral Corrosion Propagation

Carbon Steel and Stainless Steel

316L stainless steel and carbon steel MEAs provided representative lateral corrosion propagation behavior from the most and least corrosion resistant materials considered for this study. As expected, the general behavior of 316L stainless steel and carbon steel during lateral propagation experiments correlated with chloride threshold and pitting factor results. From this finding, it is suitable to further comment on the lateral corrosion propagation behavior of 2101 and MMFX-2. Based corrosion initiation and pitting factor rankings, the corrosion resistance of 2101 and MMFX-2 falls in the spectrum established between carbon steel and 316LN stainless steel. Therefore, it can be predicted that the lateral propagation behavior of 2101 would tend towards 316LN stainless steel and MMFX-2 would be more like carbon steel. 2101 had a higher resistance to corrosion initiation during chloride threshold testing than MMFX-2, but once initiated possessed a morphology of attack similar to MMFX-2, observed during pitting factor testing. Generation of new initiation sites from existing sites and thus corrosion spreading would likely occur more readily on 2101 than 316LN. However, 2101 could also be expected to have a higher resistance to lateral corrosion propagation from acidified pit solution than MMFX-2 based on the Cr content and resulting electrochemical behavior in acid solution.MMFX-2 had a similar chloride threshold to carbon steel. However, during pitting factor testing MMFX-2 demonstrated a relatively higher aspect ratio of corrosion damage morphology. Speculatively, MMFX-2 would be similar but somewhat more resistant to lateral corrosion spreading than carbon steel. From these assumptions and the results from 316L and carbon steel MEA testing, a relative ranking of rebar materials based on their resistance to lateral corrosion spreading is obtained (from most to least resistant):

316LN stainless steel > 2101 duplex stainless steel > MMFX-2 > Carbon Steel

Engineering Implications of Corrosion Propagation Behavior

The corrosion propagation behavior as well as the morphology of attack directly affect the propensity for concrete cracking. In one study on carbon steel bars, it was found empirically that the critical depth of attack required to crack concrete, X_{crit}, was a function of the rebar radius, R, and concrete cover thickness, C, as well as the length of anodic region along the axis of the bar, L (Torres-Acosta and Sagüés, 2000). Specifically, X_{crit} is proportional to the first power of $[C/2R]$ and to square of $[C/L +1]$. Hence, as the length of anodic region of corrosion propagation, L, increases, the critical depth of attack, X_{crit} decreases. This implies that both the depth of corrosion penetration, r, and the lateral area of corrosive attack, L, are important coupled factors determining the risk of concrete cracking. An example of the effect of anode length L on the critical depth of attack (X_{crit}) is presented in Figure 33 based on the empirical equation developed by Torres-Acosta and Sagüés (Torres-Acosta and Sagüés, 2000). In Figure 33, the rebar radius R is assumed to be 10 mm with a concrete cover depth of 50 mm. The lifetime of a concrete structure exposed to chlorides is determined by the time required to achieve the critical depth of corrosion attack (X_{crit}) required to cause cracking.
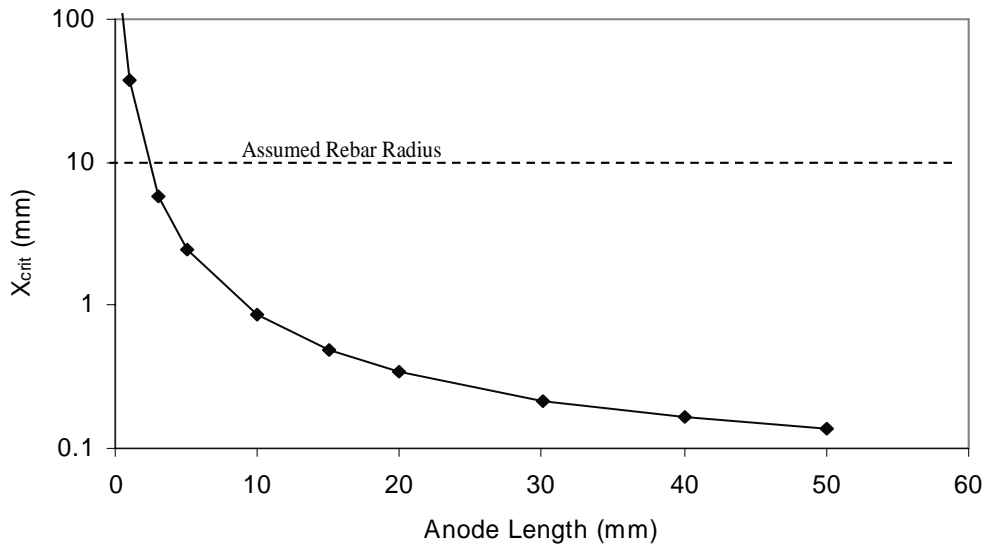
Figure 33. **Critical rebar corrosion attack depth (X_{crit}) required to damage concrete as a function of the anode length (L), based on the empirical equation developed by Torres-Acosta and Sagüés (Torres-Acosta and Sagüés, 2004). The rebar radius was assumed to be 10 mm and the concrete cover assumed to be 50 mm.**

In light of this, good candidate corrosion resistant reinforcing materials posses a high intrinsic resistance to chloride induced corrosion initiation, form pits with small anode lengths (L), and have a slow radial propagation rate (*dr/dt*). In order to extend the lifetime of concrete structures, the corrosion morphology and the propagation rate per unit area must be understood for different rebar compositions. Based on the above criteria, stainless steels are good candidates since corrosion propagation (*dr/dt*) would approach zero as stainless steel readily repassivates at rather positive potentials. In this study, it was seen that stainless steel is very resistant to stable active corrosion and corrosion spreading across the electrode surface. When attack does occur, the damage is confined to localized, deep pits. Therefore, L would remain small if propagation occurred. Therefore, X_{crit} would then be large (as seen in Figure 33) and it would be difficult to achieve corrosion induced spalling of concrete. Alternately, carbon steel was found to be much more susceptible to global depassivation once corrosion was initiated. Therefore, X_{crit} would then be small.

To better conceptualize the relationship between corrosion propagation behavior and resultant concrete cracking, it is beneficial to consider a couple of mock scenarios, utilizing results presented previously above. From the relationship between the critical depth of attack (X_{crit}) and anode length L presented in Figure 33, the time required for radial corrosion to reach a depth of X_{crit} can be calculated. Based on interpretation of lateral and radial propagation experiment results the following assumptions are made regarding the anode depth and length:

- For 316LN stainless steel, which exhibited highly localized attack, a value of L/X_{crit} = 4 is assumed. This assumption yields an X_{crit} value ≈ 2.34 mm (from Figure 33).

46

This analysis also assumes the corrosion product molar volume is the same as carbon steel and that the L/X$_{crit}$ curve in Figure 33 applies to all materials.

- Carbon steel is prone to lateral propagation based on MEA testing, and based on pitting factor testing results compared to 316LN stainless steel, a value of L/X$_{crit}$ = 40 can reasonably be assumed (10 times that of 316LN stainless steel), yielding X$_{crit}$ ≈ 0.56 mm.

- The corrosion propagation behavior of 2101 and MMFX-2 was intermediate between that of 316LN stainless steel and carbon steel. From the relative propagation rankings L/X$_{crit}$ = 8 (X$_{crit}$ ≈ 1.52 mm) is assumed for 2101 and L/X$_{crit}$ = 20 (X$_{crit}$ ≈ 0.86 mm) for MMFX-2.

For the first scenario, the potential of the rebar embedded in concrete is presumed to be 0.0 (V) vs. SCE. At this potential all rebars are susceptible to ohmically controlled radial corrosion (i.e., this potential is above the "shut-off" potential for radial growth, Table 9). The time required to reach X$_{crit}$ can be calculated via $r = kt^{1/3}$ (*eqn. 9*) using the respective *k* factor value in concrete at 0.0 (V) vs. SCE (Figure 32) for each rebar composition. The predicted corrosion propagation duration results, neglecting the initiation period, are summarized in Table 11. 316LN has the longest propagation period of 24.4 years before spalling, over 21 times greater then for carbon steel. 2101 shows an improvement of nearly 8 times greater than carbon steel. The time required to reach X$_{crit}$ for carbon steel and MMFX-2 is similar under these conditions.

For the second scenario all assumptions made for the first scenario are held. However, the rebar is considered to be at a potential of -0.35 (V) vs. SCE. 316LN and 2101 are not susceptible to further radial corrosion propagation since it is below their model "shut-off" potential in concrete at this potential (see Table 9). The results for carbon steel and MMFX-2 are summarized in Table 12. At the lower potential assumed in the second scenario (-0.35 (V) vs. SCE) the propagation period for MMFX-2 is improved by a factor of 10 over the first scenario. Carbon steel exhibited only a moderate increase in the time required to reach X$_{crit}$. For 316LN stainless steel and 2101 LDX, the time required to reach X$_{crit}$ can be considered infinite since the radial corrosion growth rate is effectively zero for the given potential.

Table 11. Theoretical time required for corrosion to propagate, at a potential of 0.0 (V) vs. SCE, to a depth of X$_{crit}$, resulting in concrete cracking.

Material	L/X$_{crit}$	Approx. X$_{crit}$ (mm)	t(yrs) to X$_{crit}$
Carbon steel	40	0.56	1.13
316LN	4	2.34	24.40
2101	8	1.52	8.92
MMFX-2	20	0.86	1.82

Table 12. Theoretical time required for corrosion to propagate, at a potential of -0.3 (V) vs. SCE, to a depth of X_{crit}, resulting in concrete cracking.

Material	L/X_{crit}	Approx. X_{crit} (mm)	t(yrs) to X_{crit}
Carbon steel	40	0.56	**2.40**
316LN	4	2.34	∞
2101	8	1.52	∞
MMFX-2	20	0.86	**18.14**

Results of the theoretical time to reach X_{crit} from the two presented scenarios are provocative for considering prospective use of corrosion resistant rebar alloys. At the more noble potentials, only 316LN stainless steel and 2101 offered a significant extension of the corrosion propagation stage. However, in the first scenario presented, 316LN still out performed 2101 by a factor of 2.7. Carbon steel had relatively short predicted propagation periods in both scenarios and the lifetime is largely dictated by the initiation period and chloride threshold. Although 316LN was the best candidate overall, the corrosion propagation period was 24.4 years (at 0.0 (V) vs. SCE), which is likely much shorter compared to the duration of the corrosion initiation period, based on chloride diffusion calculations. Materials such as MMFX-2, which possess corrosion propagation characteristics slightly better than carbon steel, must be considered carefully. When more noble potentials are encountered, the propagation period may be equivalent to that of carbon steel. However, at lower potentials there is an increase in predicted time to cause concrete cracking. It seems that the greatest possible benefit during the corrosion propagation stage is the inherent resistance to radial propagation when repassivation occurs, characterized by the "shut-off" potential.

The conversion of metal into corrosion product(s) at the rebar interface produces stress on the surrounding concrete. The analysis considered here used the carbon steel data of Torres-Acosta and Sagüés and neglected any differences in oxide molar volume between the different materials (Torres-Acosta and Sagüés, 2000). The accumulation rate of products, their crystal structure, and hence molar volume of corrosion products together are additional factors determining the possible extent of concrete damage. The propagation rate determines the metal-to-oxide conversion rate, while the oxide crystal structure, density (g/cm^3), and molar volume of the corrosion products aid in determination of the propensity to damage and crack concrete. Therefore, the molar volume of corrosion products should also be considered before endorsing any candidate corrosion resistant reinforcing material. This issue is addressed in the final section of this report and it was found that the oxide molar volume of corrosion products is similar for all materials tested. Additionally, any significant conversion of alloying elements present in corrosion resistant rebar into oxides would likely posses no additional threat to concrete cracking since their specific volume is very similar to those from carbon steel rebar. Stainless steel exhibits much more localized corrosion attack compared to carbon steel and would be expected to generate a smaller lateral accumulation (L) of corrosion products. Thus, X_{crit} would be larger in order to damage concrete. Moreover, there is no reason to believe that the curve generated in Figure 33 would differ for stainless steel since the oxide molar volumes are similar. Therefore,

stainless steel materials would be much less likely to damage concrete structures from the propagation perspective.

CONCLUSIONS

- The chloride thresholds obtained from the potentiostatic lab method using $Ca(OH)_2$ + NaCl solutions were consistent with relevant literature for carbon steel (ASTM A615). A chloride threshold of $0.25 < Cl^-/OH^- < 0.34$ was obtained during incremental chloride-addition tests of ASTM A615 steel. A slightly lower result of a Cl^-/OH^- ratio of 0.049 was found during constant-chloride testing using the potentiostatic method. *Therefore, it is concluded that chloride thresholds determined from this laboratory test approach are relevant yet conservative indications of the levels to be expected for materials in concrete.*

- A threshold Cl^-/OH^- ratio of 20 was found for un-aged pickled 316LN stainless steel (UNS S31653) during potentiostatic incremental chloride-addition testing. In contrast, un-aged, pickled 2101 LDX (UNS S32101) had a threshold Cl^-/OH^- ratio of 9.7 and un-aged, pickled MMFX-2 (Fe-9.3% Cr) had a threshold Cl^-/OH^- ratio of 4.9. *Therefore, significant improvements can be expected with highly alloyed corrosion resistant rebar materials and some improvement is possible with a Fe-9% Cr alloy.*

- Aging in the $Ca(OH)_2$ environment prior to initiation improves the chloride threshold and most of the significant aging occurs during the first few days with or without the presence of chloride. The chloride threshold for carbon steel increased from a Cl^-/OH^- ratio of 0.05 to a Cl^-/OH^- ratio of 0.15, MMFX-2 increased from a Cl^-/OH^- ratio of 0.10 to a Cl^-/OH^- ratio of 0.34, and 316LN increased from a low Cl^-/OH^- value of 20 to a Cl^-/OH^- ratio of 100 with artificial aging for 3 days at +200 mV vs. SCE. *Thus, it can be concluded that oxide aging improves chloride thresholds by degree but does not change the expected ranking of materials from best to worst.*

- Intact 316L stainless steel clad (S31603) rebar had a threshold Cl^-/OH^- ratio of 4.9. Any defect in the cladding that exposed the carbon steel core, lowered the chloride threshold to approximately that of carbon steel in the potentiostatic method. *Thus, defects in clad stainless steel rebar (whether or not they penetrate the cladding layer) degrade its corrosion initiation resistance in the corrosion threshold type test used relative to solid stainless steel.*

- The chloride threshold concentrations of highly alloyed rebar materials with mill scale present, which produces a chromium depleted surface layer, was comparable to carbon steel. *Hence, mill-scale removal is highly recommended when considering stainless steel rebar since presence of mill-scale negates the benefits of using stainless steel.*

- Simulations of chloride penetration into concrete predicted that *the time until chloride induced corrosion initiation could be extended from 8 years (for carbon steel) to 103 years (for 316LN stainless steel) for concrete structures exposed to periodic dosing with de-icing salts.*

- Once activated the time dependence of depth of radial attack, *r*, is described by $r = kt^{1/3}$, where *t* is time and *k* is a function of the chloride content of the concrete and is ohmically

limited for each material. Thus, the propagation rate was shown to be slower in concrete possessing a higher ionic resistance.

- Radial active corrosion propagation was effectively stopped when the material dependent k value dropped below 4×10^{-4} cm/sec$^{1/3}$. For 316LN stainless steel this occurred at potentials more negative than -0.2 V vs. SCE. 2101 LDX duplex stainless steel was slightly less resistant with penetration arrested at -0.35 V vs. SCE. The potential dependency of radial corrosion growth was similar for MMFX-2 and carbon steel and corrosion propagation was arrested at potentials below -0.55 V vs. SCE on both materials. *Therefore, it can be concluded that propagation of corrosion once activated would tend to repassivate on highly alloyed stainless steels unless extremely aggressive conditions (i.e., oxidizing potentials) existed in service in concrete.*

- Highly alloyed stainless steel (e.g., 18%Cr) was also very resistant to lateral corrosion spreading compared to carbon steel (ASTM A 615), on which spreading occurred rapidly in both electrochemical conditions tested (natural and activated corrosion). Similarly, a stainless steel clad alloy with a defect would be expected to resist widespread depassivation. Corrosion spreading behavior on 2101 LDX duplex stainless steel is believed to be similar to 316LN stainless steel. MMFX-2 (Fe-9% Cr) behaved similarly to carbon steel. The morphology of attack during pitting factor determination tests also followed a similar trend as mentioned above; stainless steel exhibited deep distinct pits, carbon steel tended toward general corrosion, and 2101 LDX and MMFX-2 were intermediate.

- The ramifications of the pitting factor results imply that materials with larger pitting factor values will require larger critical depths of attack, X_{crit}, given their small anode lengths in order to cause concrete damage such as cracking. In fact, theoretical calculations of the time required to reach X_{crit} confirm that 316LN stainless would likely have the longest corrosion propagation period (24.4 years at 0.0 (V) vs. SCE) of all bars considered. MMFX-2 and carbon steel had similar but much shorter propagation periods until damage (1.82 and 1.13 years respectively) while 2101 LDX was intermediate at 8.92 years. At a more negative potential, -0.35 (V) vs. SCE, MMFX-2 out-performed carbon steel by a factor of 7.6 with a propagation period of 18.14 years. 2101 LDX and 316LN were not considered at the more active potential since repassivation of chloride induced corrosion is likely on both materials at this potential, yielding an effective infinite propagation period provided the concrete remains sound.

- *Similar corrosion products were seen on carbon steel, MMFX-2, 2101 LDX stainless steel, and 316LN stainless steel.* Moreover, the literature suggests that the corrosion products based on oxides of the alloying elements will not have radically different partial molar volumes. Therefore, these corrosion products should not be expected to present a radical change from existing carbon steels concerning their ability to damage concrete. *The benefit of the corrosion resistant materials lies in the reduced surface area over which corrosion would be expected resulting in less chance of concrete damage by corrosion product wedging even if corrosion ever was initiated.*

RECOMMENDATIONS

The conclusions of this study indicate in conservative lab testing that solid 316LN stainless steel (UNS S31653) concrete reinforcement materials will exhibit practically infinite time period to initiation of chloride induced corrosion given reasonably good concrete properties and will be difficult to sustain propagation. Furthermore, results of propagation studies indicate that propagation either would be difficult to sustain or would occur over such limited areas that damage to the concrete structure via spalling due to corrosion product wedging would be difficult. Furthermore, compilation of oxide volume data suggests that oxide properties such as volume per mole of oxide formed will be similar between a 300 series stainless steel and carbon steel. *Therefore, taken all together, the results indicate the VDOT Structures and Bridge Division should strongly consider 316LN (UNS S31653) stainless steel reinforcing as a viable low corrosion related maintenance option for the most critical applications faced in roadway and bridge applications.* For instance, metropolitan applications with limited access and repair opportunities would benefit the most from such materials. In addition, it is strongly recommended that the 316LN should always be used in a pickled condition free of mill-scale in order to enjoy the benefits of this material. The pickling should be specified in the purchase order and no subsequent high temperature heat treatment should be imposed.

Solid duplex stainless steel 2101 LDX (UNS 32101) indicated substantially inferior corrosion resistance compared to 316LN but improved relative to carbon steel. Given the substantial cost investment required in the initial acquisition of this material the absence of superior corrosion resistance calls its cost effectiveness into question. The poor corrosion performance compared to 316LN is unclear and is not predicted from the PREN (pitting resistance equivalency number) of this material. *Until possible problems with heat treatments and unintended detrimental metallurgical phase formation are resolved, this material is not recommended to VDOT. In addition, the VTRC should investigate the cause of inferior corrosion performance or at least procure additional material for further corrosion evaluations. Moreover, this material should be pickled by the manufacturer since the presence of mill scale has been shown to be detrimental to the corrosion resistance of highly alloyed bars.*

A lower cost option would be to consider a high alloyed (e.g., 18% Cr) stainless steel clad rebar material such as UNS 31603. It should be noted that the clad rebar material always exhibited initiation at far lower chloride threshold concentrations than the solid 316LN material. This was due to the high probability of the presence of some defect in the clad material that inadvertently exposed the carbon steel core. However, clad materials also showed evidence of limited propagation that might limit concrete damage via the oxide wedging mechanism. Specifically, corrosion initiated at defects that exposed carbon steel (i.e., seams, cut ends, capped ends, etc.) but corrosion did not propagate onto the stainless steel. No specific advice is given concerning which method should be used to cover cut ends. However, it can be assumed that stainless steel clad rebar will readily exhibit initiation of chloride induced corrosion much like plain carbon steel but experience limited propagation onto the stainless steel. Possible severe corrosion propagation within the carbon steel core was not thoroughly investigated in this study and is recommended as a topic for further study so that the advantages and disadvantages of this material are fully understood. *The VTRC should consider further corrosion propagation studies of the stainless steel clad rebar in concrete ponded with NaCl solution with various defects in the cladding such as holes and cut ends.* One possible advantage to be noted for the clad material is

that the galvanic couple between an activated carbon steel core and stainless steel clad surface is no worse and may not be as detrimental as a galvanic coupling to carbon steel. Therefore, it is recommended that additional corrosion propagation studies be conducted on clad rebar with cut ends above the chloride threshold in order to examine fully the ramifications of corrosion propagation of the steel core on the integrity of concrete structures. Otherwise, this material option remains a viable low cost alternative to carbon steel and might be considered even for "high use/low access" applications.

Another low cost option is the MMFX-2 (Fe-9% Cr bainitic steel). This material exhibited slightly improved chloride corrosion thresholds compared to plain carbon steel in a variety of tests and would not be as expensive as a Fe-18%Cr-8%Ni stainless steel (i.e., UNS 31653). It should be noted that the material was delivered in a non-pickled condition and that in this condition, the material was not better than carbon steel (ASTM A615) in the laboratory chloride threshold initiation tests. It should be noted that the performance of this material is improved over carbon steel in initiation tests in a pickled condition (i.e., Cl$^-$ thresholds expressed as Cl$^-$/OH$^-$ level approaching 4.9) but did not approach the chloride threshold of a highly alloyed stainless steel. This material was also found to be better than carbon steel in testing conducted in concrete blocks ponded with saltwater solutions by Clemeña. It should be noted that large areas of chloride induced corrosion would likely spread across the surface of this material much like in the case of carbon steel and corrosion products were found to be of similar identity. Therefore, from the propagation perspective, corrosion induced wedging and concrete damage might be just as prevalent once initiated on MMFX-2 as in the case of the carbon steel albeit with a slightly higher chloride threshold. *The VTRC should consider further testing of MMFX-2 in concrete ponded with NaCl solution, including bars in the pickled condition.* Should a slightly elevated chloride threshold be obtained, this material is a low cost alternative to ASTM 615 that might serve well in rural or low use high value applications such as rural bridges. *Based on this research, it is recommended that if the VDOT Structure and Bridge Division use the MMFX-2 bars, it should be used in the pickled condition to maximize any possible gain in corrosion resistance.*

Finally, some of the electrochemical test methods used during this study can be carried out over a relatively short period of time. This is particularly true if these electrochemical tests are compared to the time required to embed alternative reinforcement in concrete, properly cure, then pond with salt water and determine the corrosion resistance. *Therefore, the VTRC should investigate whether the electrochemical test methods used during this study could be used by the VDOT Materials Division to evaluate the corrosion resistance of future candidate reinforcing bars.*

COSTS AND BENEFITS ASSESSMENT

The cost trade-off to be confronted in the choice of alternative rebar materials centers upon the initial acquisition costs compared to the life-cycle and repair costs associated with the use of a given reinforcement material. The corrosion resistant materials studied offer the chance for reduced life-cycle costs compared to the incumbent plain carbon steel but will be up to 8 times more expensive to purchase. This is particularly true in the more costly pickled condition

that must be specified in the case of all corrosion resistant materials to be considered. The benefit of the alternative corrosion resistant material would lie in its reduced life cycle costs and/or extended period of performance or both to generate a total cost savings given the fact that acquisition costs may be great. The average cost of plain carbon steel rebar is .32$/lb and the time until corrosion initiation (Table 7) might only be several years under harsh dosing. The time until propagation-induced damage may only be 2.4 additional years (Table 12). At this point yearly maintenance cost must be factored in. The cost of epoxy coated steel is only slightly higher at 0.42 - 0.47 $/lb, but the added value is often debated. In the case of 316LN stainless steel (UNS S31653), the time until initiation approaches infinity on a bridge given a deicing cycle of less than 100 days per year and is as high as 100 years for a conservative 120 days of yearly dosing. Additionally, the time of propagation until damage may be 25 years or more (Tables 11 and 12). In this case, the life cycle costs may be reduced to zero or close to a minimum, since no extra maintenance would be required. The initial acquisition costs of 316LN stainless steel would be 1.61 $/lb, but there might be zero corrosion related maintenance costs. The case of the clad stainless steel is even more interesting, the cost drops to 1.09 $/lb and the time until initiation might be less than for solid stainless steel but recommended studies could show that it is quite difficult to damage concrete owing to the small areas exposed at defects. The case of the MMFX-2 steel (Fe-9% Cr) is more curious. Here, the chloride induced corrosion threshold is marginally improved leading to some possible reduction in life cycle costs but with greater acquisition costs compared to ASTM A 615. The margin is a lot less clear with an initial cost of 0.58 $/lb and a gain in initiation time from 4 to 8 years (Table 7). Therefore, the benefits of the slightly improved corrosion resistance must be weighed against the added costs of maintenance that might start after a 4-year delay on a heavily salted bridge.

Finally, to put the cost of using alternative reinforcement in proper perspective, an approach by Brown et al., converted the cost per pound of reinforcement to the cost per square foot of bridge deck area (Brown et al., 2003). This was done to understand better the life-cycle cost by providing a means to compare the construction cost to the possible rehabilitation cost. Using a similar approach as Brown, et al., Table 13 was created, which provides a cost comparison for the different types of reinforcement per bridge deck surface area. If the cost suggested by Brown, et al., to rehabilitate a bridge deck with an overlay (includes overlay materials, concrete removal, and traffic control) is adjusted using an interest rate of 2%, the current estimated rehabilitation cost would be $12.93/ft^2. Most likely the cost to install the bars would be less than $4.88/ft^2, which is the difference in cost between the 316LN bar and placement of the overlay. Therefore, the use of any of these bars would be a cost effective choice if the bridge deck requires an overlay before it reaches the design life of the structure. Furthermore, if pickling is required, the additional cost is relatively small with acid pickling costing between 0.04 – 0.05 $/lb (for the 316LN this would only increase the material cost to 8.30 $/ft^2). Clearly, all of these suggestions are reasonable options if future rehabilitation costs are considered.

Table 13. Cost for Alternative Deck Reinforcement

Rebar Type	Material Cost ($/lb)	Material Cost ($/ft^2)
Carbon Steel	0.32	1.60
Clad Layer	1.09	5.45
MMFX-2	0.58	2.90
316LN	1.61	8.05

ACKNOWLEDGMENTS

REFERENCES

ACI Committee 201, Guide to Durable Concrete Manual of Concrete Practice Part 1. American Concrete Institute, Detroit, 1994.

ASTM A923-01 Detecting Detrimental Intermetallic Phase in Wrought Duplex Austenitic/Ferritic Stainless Steels, ASTM International, West Conshohocken, PA, 2001.

Abreu, C. M., Cristobal, M. J., Novoa, X. R., Pena, G., and Perez M. C. Long-Term Behavior of AISI 316L Passive Layer in Chloride Containing Medium. *Electrochemica Acta*, Vol. 51, 2006, pp. 1881-1890.

Alonso, C., Andrade, C., Castello, M., and Castro, P. Chloride Threshold Values to Depassivate Reinforcing Bars Embedded in a Standardized OPC Mortar. *Cement and Concrete Research*, Vol. 30, 2000, pp. 1047-1055.

Bentur, A., Diamond, S., and Berke, N. S. *Steel Corrosion in Concrete*. London, E & FN Spon, an imprint of Chapman & Hall, London, UK., 1997.

Bentz, D. P., Clifton, J. R., and Snyder, K. A. Predicting the Service Life of Chloride Exposed Steel-Reinforced Concrete. *Concrete International*, Vol. 18, No. 12, 1996, pp. 42-47.

Bertolini, L., Bolzoni, F., Pastore, T., and Pedeferri, P. Behaviour of Stainless Steel in Simulated Concrete Pore Solution. *British Corrosion Journal*, Vol. 31, No. 3, 1996, pp. 218-222.

Bertolini, L., Elsener, B., Pedeferri, P., and Polder, R. *Corrosion of Steel in Concrete*. Weinheim, Wiley-VCH Verlag GmbH & Co, 2004.

Brown, M. C., Weyers, R. E., and Wheeler, M. C. *Corrosion Protection Service Life of Epoxy-Coated Reinforcing Steel in Virginia Bridge Decks*. FHWA/VTRC 04-CR7. Virginia Department of Transportation, Richmond, VA, 2003.

Budiansky, N. D., Bocher, F., Cong, H., Hurley, M. F., and Scully, J. R. Use of Coupled Multi-Electrode Arrays to Advance the Understanding of Selected Corrosion Phenomena. In *Corrosion 2006* San Diego. NACE International, Houston, 2006.

Budiansky, N. D., Hudson, J. L., and Scully, J. R. Origins of Persistent Interactions among Localized Corrosion Sites on Stainless Steel. *Journal of Electrochemical Society*, Vol. 151, 2004, pp. B233-243.

Clear, K. C. Effectiveness of Epoxy-Coated Reinforcing Steel C-SHRP Report: Executive Summary. *Transportation Research Circular,* Vol. 403, 1996, pp. 66.

Davenport, A. J., and Lee B. K. Passive Film Growth Kinetics for Iron and Stainless Steel. *Electrochemical Society Proceedings* Vol. 13, 2002, pp. 187-197.

Goni, S., and Andrade C. Synthetic Concrete Pore Solution Chemistry and Rebar Corrosion Rate in the Presence of Chlorides. *Cement and Concrete Research,* Vol. 20, 1990, pp. 525-539.

Gouda, V. K., and Halaka, W. Y. Corrosion and Corrosion Inhibition of Reinforced Steel. *British Corrosion Journal,* Vol. 5, 1970, 204-208.

Gu, P., Elliot, S., Beaudoin, J. J., and Arsenault, B. Corrosion Resistance of Stainless Steel in Chloride Contaminated Concrete. *Cement and Concrete Research,* Vol. 26, No. 8, 1996, pp. 1151-1156.

Hausmann, D. A. Steel Corrosion in Concrete. How Does it Occur? *Journal of Materials Protection,* Vol. 6, No. 19, 1967, pp. 19-23.

Houston, J. T., Atimay, E., and Ferguson, P. M., *Corrosion of Reinforcing Steel Embedded in Structural Concrete.* CFHR-3-5-68-112-1F Center for Highway Research at the University of Texas, Austin, 1972.

Hunkler, F. The Resistivity of Pore Water Solution--A Decisive Parameter of Rebar Corrosion and Repair Methods. *Construction and Building Materials,* Vol. 10, No. 5, 1996, pp. 381-389.

Hunkler, F., and Bohni, H. Determination of Pit Growth Rates on Aluminum Using a Metal Foil Technique. *Corrosion,* Vol. 28, No. 1, 1981, pp 645.

Hurley, M. F. *Critical Issues Regarding the Corrosion Behavior of Stainless Steel Clad Rebar.* Master's Thesis, University of Virginia, Charlottesville, 2002.

Hurley, M. F., and Scully, J. R. Chloride Threshold Levels in Clad 316L and Solid 316LN Stainless Steel Rebar. In *Corrosion 2002* Denver. NACE International, Houston, 2002.

Hurley, M. F., Scully, J. R., and Clemeña, G. Selected Issues in the Corrosion Resistance of Stainless Steel Clad Rebar. In *Corrosion 2001* Houston. NACE International, Houston, 2001.

Jones, D. A. *Principals and Prevention of Corrosion.* Prentice-Hall, Inc., Upper Saddle River, NJ, 1996.

Koch, G. H., Brongers, M. H., Thompson, N. G., Virmani, Y. P., and Payer, J. H. *Corrosion Cost and Preventive Strategies in the United States.* FHWA-RD-01-156. Federal Highway Administration, Mclean, VA, 2001.

Li, L., and Sagüés, A. A. Chloride Corrosion Threshold of Reinforcing Steel in Alkaline Solutions-Open-Circuit Immersion Tests. *Corrosion,* Vol. 57, No. 1, 2001, pp. 19-28.

Li, L.-F., Caenen, P., Daerden, M., Vaes, D., Meers, G., Dhondt, C., and Celis, J.P. Mechanism of Single and Multiple Step Pickling of 304 Stainless Steel in Acid Electrolytes. *Corrosion Science,* Vol. 47, 2004, pp. 1307-1324.

Lide, D. R., (Ed.). *CRC Handbook of Chemistry and Physics.* Taylor and Francis, Boca Raton, FL, 2005.

Lysogorski, D. K., Cros, P., and Hartt, W. H. Performance of Corrosion Resistant Reinforcement as Assessed by Accelerated Testing and Long Term Exposure in Chloride Contaminated Concrete. In *Corrosion 2005* Houston. NACE International, Houston, 2005.

Mammoliti, L. T., Brown, L. C., Hansson C. M., and Hope, B. B. The Influence of Surface Finish of Reinforcing Steel and pH of Test Solution on the Chloride Threshold Concentration for Corrosion Initiation in Synthetic Pore Solutions. *Cement and Concrete Research,* Vol. 26, No. 4, 1996, pp. 545-550.

McDonald, D. B., Pfeifer, D. W., and Blake, G. T., *The Corrosion Performance of Inorganic-, Ceramic-, and Metallic-Clad Reinforcing Bars and Solid Metallic Reinforcing Bars in Accelerated Screening Tests.* FHWA-RD-96-085. Federal Highway Administration, McLean, VA, 1996.

McDonald, D. B., Pfeifer, D. W., and Sherman, M. R. *Corrosion Evaluation of Epoxy-Coated, Metallic-Clad and Solid Reinforcing Bars in Concrete.* FHWA-RD-98-153. Federal Highway Administration, McLean, VA, 1998.

MMFX Product Bulletin, MMFX Steel Corporation of America, 2001.

Montemor, M. F., Simoes, A. M. P., and Ferreira, M. G. S., Analytical Characterization of the Passive Film Formed on Steel in Solutions Simulating the Concrete Interstitial Electrolyte. *Corrosion,* Vol. 54, No. 5, 1998, pp. 347-353.

Newman, R. C., and Franz, E. M. Growth and Repassivation of Single Corrosion Pits in Stainless Steel. *Corrosion,* Vol. 40, No. 7, 1984, pp. 325-330.

Nurnberger, U., (Ed.). *Stainless Steel in Concrete*. European Federation of Corrosion Publications Number 18, Institute of Materials, London, 1996.

Olsson, C.-O. A., and Landolt, D., Passive Films on Stainless Steels-Chemistry, Structure and Growth. *Electrochemica Acta,* Vol. 48, pp. 1093-1104.

Polder, R. B., and Peelen, H. A. Characterization of Chloride Transport and Reinforcement Corrosion in Concrete Under Cyclic Wetting and Drying by Electrical Resistivity. *Cement and Concrete Composites,* Vol. 24, 2002, pp. 427-435.

Pourbaix, M. *Atlas of Electrochemical Equilibra in Aqueous Solutions.* National Association of Corrosion Engineers, Houston, TX, 1974.

Renner, M., Heubner, U., Rockel, M. B., and Wallis, E. Temperature as a Pitting and Crevice Corrosion Criterion in the FeCl$_3$ Test. *Werkstoffe und Korrosion,* Vol. 37, 1986, pp. 183-190.

Ryell, J. and Richardson B. S. *Cracks in Concrete Bridge Decks and Their Contribution to Corrosion of Reinforcing Steel and Prestressed Cables.* IR51. Ontario Ministry of Transportation and Commission ,Ontario, Canada, 1972.

Scully, J. R., Marks, C. A., and Hurley, M. F. *Testing of Selected Metallic Reinforcing Bars For Extending Service Life of Concrete Bridges in Solutions.* FHWA/VTRC 03-CR11 Federal Highway Administration, Mclean, VA, 2003.

Sedriks, J. A. *Corrosion of Stainless Steels.* Princeton, John Wiley & Sons, Inc., NJ, 1996.

Stott, F. and Wei F. I. High Temperature Oxidation of Commercial Austenitic Stainless Steels. *Materials Science Technology,* Vol. 5, 1989, pp. 1140-1147.

Szklarska-Simialowska, Z. *Pitting and Crevice Corrosion.* NACE, Houston, TX, 2005.

Torres-Acosta, A. A., and Sagüés, A. A. Concrete Cover Cracking with Localized Corrosion of Reinforcing Steel. In *Proceedings Fifth CANMET/ACI*, V.M. Malhotra (Ed.). ACI International, Barcelona, Spain, 2004, pp. 591-612.

Torres-Acosta, A. A., and Sagüés, A. A. Concrete Cracking by Localized Steel Corrosion-Geometric Effects. *ACI Materials Journal,* Vol. 101, No. 6, 2004, pp. 501-507.

Tuutti, K. *Corrosion of Steel in Concrete.* Swedish Cement and Concrete research Institute, Stockholm, 1982.

Veleva, L., Alpuche-Aviles, M. A., Graves-Brook, M. K., and Wipf, D. O. Comparative Cyclic Voltammetry and Surface Analysis of Passive Films Grown on Stainless Steel 316 in Concrete Pore Model Solutions. *Journal of Electroanalytical Chemistry,* Vol. 537, 2002, pp. 85-93.

Veleva, L., Alpuche-Aviles, M. A., Graves-Brook, M. K., and Wipf, D. O. Voltammetry and Surface Analysis of AISI 316 Stainless Steel in Chloride-Containing Simulated Concrete Pore Environment. *Journal of Electroanalytical Chemistry,* Vol. 578, 2005, pp. 45-53.

Wilde, B. E. A Critical Appraisal of Some Popular Laboratory Electrochemical Tests for Predicting the Localized Corrosion Resistance of Stainless Alloys in Sea Water. *Corrosion,* Vol. 28, No. 8, 1972, pp. 283-291.

Wong, K. P. and Alkire, R. C. Local Chemistry and Growth of Single Corrosion Pits in Aluminum. *Journal of the Electrochemical Society,* Vol. 137, No. 10, 1990, pp. 3010.

Yonezawa, T., Ashworth, V., and Procter, R. P. M. Pore Solution Composition and Chloride Effects on the Corrosion of Steel in Concrete. *Corrosion,* Vol. 44, No. 7, 1998, pp. 489-499.